Journal of Materials Research and Technology 31 (2024) 3489–3508

Contents lists available at ScienceDirect

Journal of Materials Research and Technology

journal homepage: www.elsevier.com/locate/jmrt

Influence of hot top geometry on columnar-to-equiaxed transition in a 12 MT steel ingot

Neda Ghodrati [a], Patrice Ménard [b], Jean-Benoit Morin [b], Mohammad Jahazi [a,*]

[a] École de Technologie Supérieure, Department of Mechanical Engineering, 1100 Notre-Dame St W, Montreal, Quebec, Canada, H3C 1K3
[b] Finkl Steel - Sorel, 100 McCarthy, Saint-Joseph-de-Sorel, QC, J3R 3M8, Canada

ARTICLE INFO

Keywords:
Hot top
Ingot casting
Solidification time
Columnar to equiaxed transition
Macrosegregation
Microporosity
Shrinkage cavity

ABSTRACT

In the present work, the impact of hot top geometry and thermal history on the Columnar-to-Equiaxed Transition (CET) point, of a 12 MT steel ingot was determined using finite element modeling. Experimental validation of the model was conducted on an industrial-size ingot, focusing on temperature, macrosegregation, and shrinkage microporosity. The anticipated Columnar-to-Equiaxed Transition point, influenced by the interaction of solid front rate, thermal gradient, and solid fraction was considered in the analysis. The findings revealed a shift in the CET position in new configurations, up to 56 mm, 63 mm, and 60 mm from the ingot wall in the bottom, middle, and top of the ingot, respectively. The changes are attributed to variations in the kinetics of solidification, particularly the solidification time. Thermo-mechanical phenomena, encompassing mold filling, cooling, solutal convection, and flow driven by shrinkage, were incorporated into the model to predict macrosegregation and the risk of porosity and shrinkage cavity formation for different hot top geometries. A criterion is proposed that allows mitigating macrosegregation and minimizing the risk of porosity and shrinkage cavity.

1. Introduction

Ingot casting is the most important production method of speciality steels which are extensively used in transportation and power transmission industries [1–4]. The cast ingots often serve as the initial form for subsequent processes such as forging, heat treatment, and machining, and ultimately shaping the final components [5]. The demand for high-quality speciality steels, especially for larger size final products, such as shafts or dies for metal forming operations, requires the production of very large size ingots. It is well-known that the as-cast microstructure is chemically and microstructurally very heterogeneous [5,6]. Solidification is a very complex multiphase and multiscale process that includes heat, momentum, mass, solute transport, and melt convection, rendering significant intricacy to predicting the as-cast structure [7,8]. The microstructure of the as-cast ingot is composed of three main zones: the chill zone, very close to the mold wall with fine equiaxed grains; the columnar zone with very long grains, oriented towards the heat extraction direction of the ingot; and the equiaxed zone which comprises of very large equiaxed grains in the central part of the ingot originating from the undercooled liquid [6,9]. One of the major sources of chemical heterogeneity, particularly, in the case of large-size cast ingots, is the formation of centerline macrosegregation which in combination with porosity and shrinkage defects could seriously reduce the quality of the final product [10]. Macrosegregation, characterized by non-uniform distribution of alloying elements, that result in microstructural heterogeneities, often resistant to elimination, even after thermo-mechanical operations. The presence of such macrosegregated zones reduces the quality and service properties of the final product [11–14]. Shrinkage porosity compromises mechanical performance in cast parts when liquid metal fails to compensate for volume contraction during solidification [1,2,5,15]. Macroscopic shrinkage cavities, akin to open pipes in the hot top region, influence macrosegregation by adjusting the position of concentrated positive segregation, impacting solidification flow dynamics [1,16].

One of the major factors affecting the occurrence and extent of the above defects is the boundary between the columnar and equiaxed zones, known as the Columnar-to-Equiaxed Transition (CET) point [6,9]. This transition signifies a transformation in solidification conditions, shifting from constrained growth to conditions that facilitate unconstrained, free growth. The columnar region promotes the occurrence of centerline segregation, cracks, and porosity [17,18]. The position of the CET varies depending on the temperature gradient that exists between

* Corresponding author.
E-mail addresses: neda.ghodrati.1@ens.etsmtl.ca (N. Ghodrati), pmenard@finkl.com (P. Ménard), jbmorin@finkl.com (J.-B. Morin), mohammad.jahazi@etsmtl.ca (M. Jahazi).

https://doi.org/10.1016/j.jmrt.2024.07.055
Received 3 May 2024; Received in revised form 27 June 2024; Accepted 12 July 2024
Available online 14 July 2024

the liquid and the solid fronts, as well as the solidification time. Therefore, it is of critical importance to determine the CET and to quantify the impact of processing parameters on its evolution. Both experimental and theoretical models have been used to study the CET evolution and predict its formation [15]. While analytical models, such as those proposed by Rappaz et al. [18], and its variants have been used by many; however, in recent years, access to advanced computational capabilities has allowed the development of numerical simulation models that take into account the complex thermal, metallurgical, and mechanical phenomena resulting in accurate determination of the influence of various casting parameters on CET evolution and its impact on casting defects.

The geometric configuration of the cast ingot setup, including the mold, hot top, sideboard, riser, runner, and trumpet, exerts a significant influence on solidification kinetics, and therefore, as the primary determinants affecting the CET [18–20]. As reported by many authors, among these factors, hot top configuration emerges as one of the most critical ones affecting the CET [3,15,21]. The hot top situated on the upper part of the mold, plays a pivotal role in feeding the ingot during casting, controlling heat flow, and providing a region for segregates and non-metallic inclusions [6]. Changes in hot top characteristics significantly affect solidification kinetics; thereby, changing the CET position [15,19,20]. Hence, modifying the hot top configuration to optimize solidification time while considering the CET can significantly improve casting quality and minimize defect formation.

Qian et al. [22], proposed an optimum hot top height and preheating temperature in order to control feeder channel segregate in the hot top and centerline shrinkage porosity in a 100-tons ingot. However, the study was focusing primarily on the feeder channel in the hot top and microporosity, and did not discuss the impact of the changes on CET position and the subsequent effect on macrosegregation. Kermanpur et al. [23], investigated the effects of hot top insulation material shape and height on solidification behavior and crack susceptibility in a 6 MT low-carbon steel ingot. They concluded that utilizing a circular hot top shape, reduced crack susceptibility during subsequent hot forging processes. However, the investigation did not extend to examining the influence of the hot top on CET or macrosegregation and porosity. Wang et al. [20] and Tashiro et al. [19] focused on the influence of hot top geometry on the elimination of shrinkage porosity steel ingots, but the influence of the hot top on CET and macrosegregation were not documented. Kumar et al. [24] investigated the impact of insulating refractory material in a 6.2 MT ingot, revealing finer axial grain structure and increased axial macrosegregation with an exothermic refractory material. They conducted experimental measurements of the columnar thickness in the hot top zone; however, the position of CET in the body was not reported. Li, Hui-Cheng et al. [25], took a different approach by applying pulsed magneto-oscillation in the hot top (HPMO). They reported that HPMO induced significant grain refinement, shorten the length of columnar grains, and reduced macrosegregation severity. However, the influence of altering the hot top configuration on the CET, macrosegregation, and shrinkage porosity was not considered.

Despite the above extensive studies, the influence of hot top configuration on CET position remains unexplored, this study aims to fill these gaps by examining the impact of various hot top designs on the CET and introducing a solidification time criterion addressing shrinkage microporosity, cavity formation, and macrosegregation. A 12 MT high-strength steel ingot is considered for the study, and the finite element code THERCAST® 3D was used to develop and simulate the solidification process, determining the correlations between CET position and the formation of defects in the as-cast microstructure.

2. Materials and methods

2.1. Experiments

The experimental procedure involved the bottom pouring of a medium carbon high-strength steel, with 0.32% C, 0.57% Mn, 0.34% Mo, 1.08% Cr, 0.23% Ni, and 0.27% Si, in weight into a 12 MT polygonal-shaped mold. The molten metal originated from an electric arc furnace, underwent ladle furnace processing and vacuum degassing. Subsequently, the molten metal was bottom-poured, at a temperature of 1580 °C and a duration of 26 min, into a cast iron mold. The hot top was integrated into the mold with its sidewalls lined with refractory material and its top surface covered with two exothermic caps. Fig. 1 illustrates the ingot casting setup (Fig. 1a and b), the hot top (Fig. 1c and d), and the ingot (Fig. 1e). During the casting and solidification processes, the mold temperature was meticulously monitored using seven strategically placed thermocouples at a depth of 25 mm inside the mold wall from the exterior surface, as illustrated in Fig. 1a. Three thermocouples were positioned in the hot top (TC1, TC2, and TC3), while the remaining four were distributed in the top (TC4), middle (TC5), and bottom parts of the mold (TC6, TC7), as outlined in Table 1. After solidification and demolding, the ingot was longitudinally cut from the center. In the subsequent steps of the experiment, the central longitudinal section, possessing a thickness of 25.4 mm, was divided into two distinct sections.

Fig. 2 illustrates the sequential steps of the cutting process. One of these sections underwent further subdivision into ten individual blocks. These blocks were subjected to a grinding process, followed by a dye penetration inspection (DPI) on each block to assess microporosity. Fig. 3 shows the presence of microporosity on the upper centerline blocks. Furthermore, the other half of the central block was cut into 370 small samples, and each sample underwent chemical measurements to create a macrosegregation map for each element. The chemical analysis of the samples was performed utilizing a Thermo Scientific ARLTM 4460 Optical Emission Spectrometer (Thermo Fisher Scientific Inc., Waltham, MA, USA). Subsequently, the segregation ratios of each sample were computed using the relation: $R^i = (w^i - w_0{}^i)/w_0{}^i$, where R^i represents the segregation ratio of solute element w^i is the solute's local concentration, and w_0^i is its initial concentration. A positive or negative value of R^i indicates positive or negative segregation, respectively. The obtained segregation ratios were instrumental in constructing macrosegregation patterns for elements across the entire longitudinal section. This mapping process was executed using MATLAB® (The MathWorks Inc., Natick, MA, USA) [26], (Carbon segregation in Fig. 2). The above methodology, though very lengthy and time-consuming, ensures a detailed understanding of the casting and solidification processes, providing valuable insights into the impact of hot top designs on the final ingot quality.

2.2. Modeling

The full-size model of the 12 MT ingot was established using the industrial bottom pour casting system (Fig. 1) as a reference. The mold cavity was 2000 mm in height, the ingot was around 1009 mm in average width in the hot top region after solidification, and 16 flutings on the exterior surface. The mold consisted of a big-end-up cast-iron taper with a 381 mm in height hot top with insulating refractory tiles lined inside, and insulating exothermic refractory board overlaid on the melt top (Fig. 4a, b, and c). For finite element modeling (FEM), a 90° model (1/4) was used according to the rotational symmetry of the 16 flutings (Fig. 4c).

2.3. FEM model setup

Three-dimensional simulations of mold filling and solidification were conducted using the finite element software THERCAST® by Transvalor S.A., Biot, France, which employs a volume-averaged solid-liquid two-phase model [27–29]. The solidification model relies on breaking down the solidification system into multiple domains. Each domain, such as the mold, hot top, or ingot, is divided into independent finite element meshes of tetrahedral form. During the filling phase, an

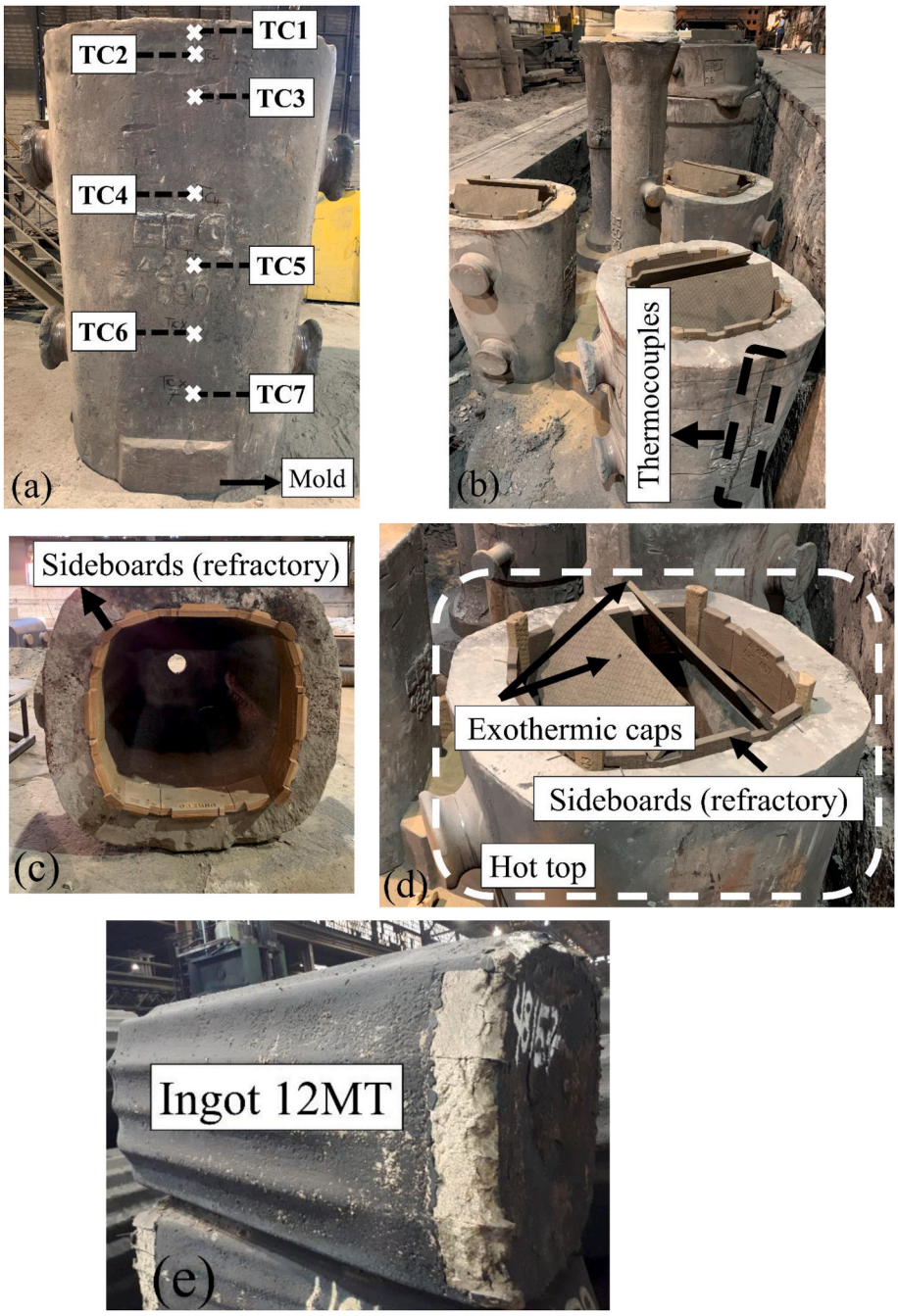

Fig. 1. Ingot casting setup for 12 MT, (a) the position of 7 thermocouples (TC1 to TC7), (b) bottom pouring ingot casting setup, (c) refractory material in the hot top, (d) the hot top, (e) 12 MT ingot.

Table 1
The position of thermocouples on the mold surface.

Number of thermocouples (TC)	Distance from the top surface of the mold
TC1	51 mm
TC2	127 mm
TC3	279 mm
TC4	686 mm
TC5	991 mm
TC6	1295 mm
TC7	1600 mm

arbitrary Lagrangian-Eulerian (ALE) formulation was employed to compute thermal convection within the liquid pool and mushy zone, as well as to track the evolution of metal volume and mass within the mold over time. However, for calculating deformation in solid regions, a Lagrangian method was utilized. Notably, the modeling did not consider sedimentation of equiaxed grains or mold deformation. To streamline the numerical models and minimize computational expenses without compromising result accuracy, several assumptions were made [21,27,29–31].

1. The liquid is modeled as Newtonian, whereas the mushy zone is characterized by a viscoplastic behavior. On the other hand, the solid zone is modeled with an elasto-viscoplastic behavior.

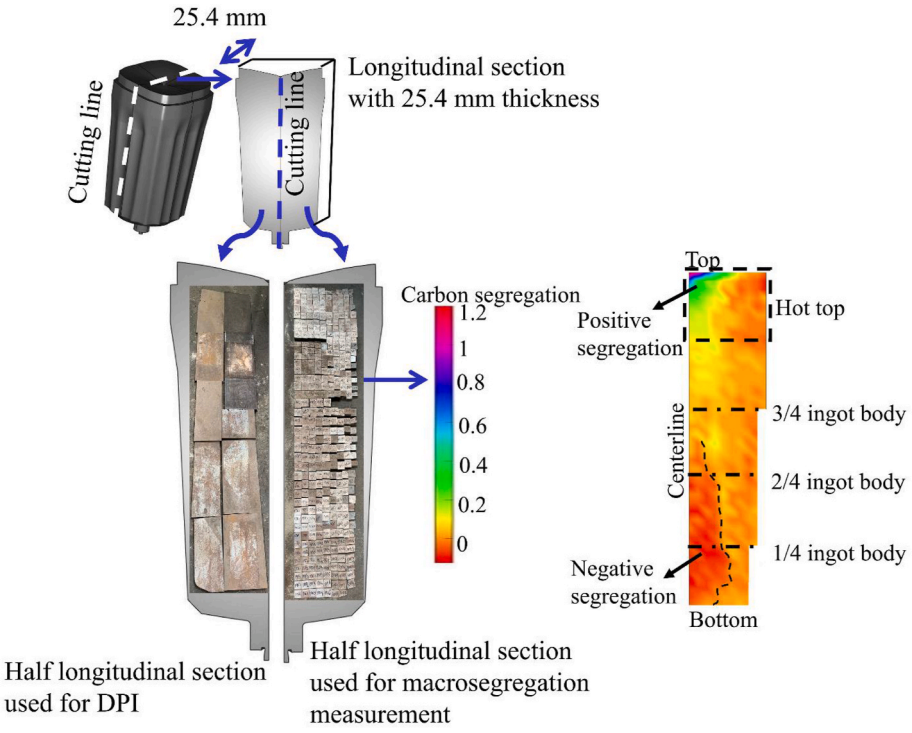

Fig. 2. Cutting plan of ingot 12 MT.

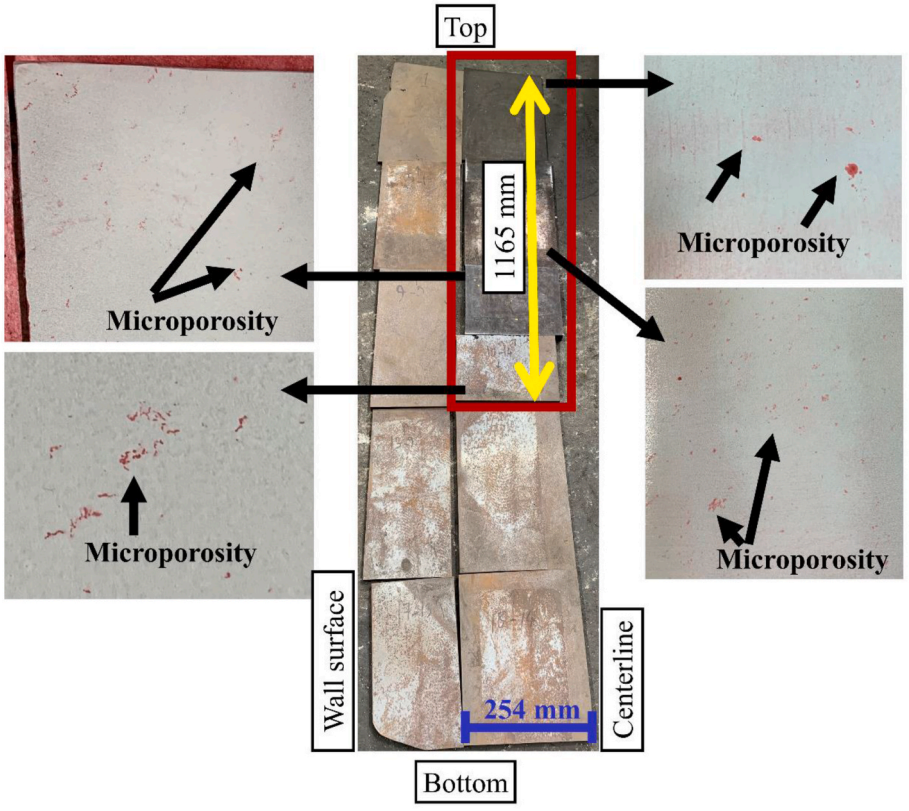

Fig. 3. Dye penetration inspection (DPI) on the half longitudinal section of real size ingot, observation of the microporosity on the upper centerline blocks.

2. The liquid was assumed to be incompressible and exhibit Newtonian behavior, while the fluid flow was presumed to be laminar due to the slow filling rate associated with the bottom pouring technique. The gravity-driven natural convection loops were formed due to local density variation, which encompassed both thermal convection flows induced by thermal expansion and temperature gradients, as well as solutal convection flows induced by solutal expansion and

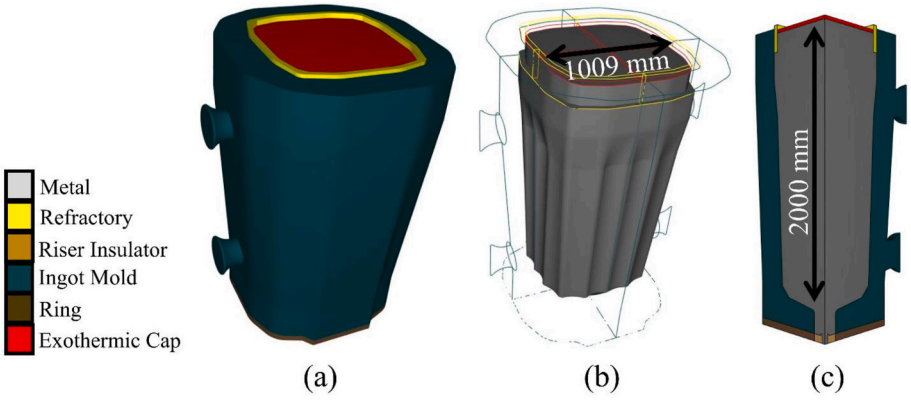

Fig. 4. Establishment of 12 MT casting models for finite element (FE) modeling: (a) model constructed based on the real casting system with; (b) representation of the ingot within the model featuring a transparent mold; (c) utilized 90° model representing 1/4 of the entire casting system.

concentration gradients [11,27,32,33]. In the momentum equation, the volumetric mass of the liquid is expressed using the equation:

$$\rho_l = \rho_0 \left(1 - \beta_T (T - T_{ref}) - \sum_{i=1}^{n} \beta_i (\omega_l^i - \omega_0^i)\right) \quad (1)$$

here, ρ_l represents the liquid density, ρ_0 denotes the density taken at the reference temperature T_{ref} (the liquidus temperature), β_T and βi are the thermal and solutal expansion coefficients, respectively. T stands for the temperature, ω_l^i represents the solute concentration in the liquid, and ω_0^i is the initial solute concentration for solute element i.

3. The mushy region was conceptualized as an isotropic porous solid medium saturated with liquid. It is assumed that the media is saturated, where $f_l + f_s = 1$, with f_l representing the volumetric fraction of the liquid and f_s representing the volumetric fraction of the solid. This is under the following equation:

$$(X) = X_l f_l + X_s f_s \quad (2)$$

The Carman-Kozeny relationship provides the isotropic permeability of the mushy zone.

$$K_{perm} = \frac{d_2^2 f_l^3}{180(1 - f_l)^2} \quad (3)$$

where d_2 is the secondary dendrite arm spacing and f_l is the liquid fraction. The isotropic permeability (K_{perm}) is contingent upon the secondary arm spacing (SDAS) value and the local liquid fraction. It is important to acknowledge that the Carman–Kozeny equation assumes the presence of a liquid fraction, resulting in a K_{perm} value that is a real number. When the liquid fraction reaches zero and the material undergoes complete solidification, its permeability becomes negligible or zero, indicating an absence of fluid flow through the solid material. Throughout solidification, the thickness of the mushy zone evolves dynamically, influenced by factors such as thermal conditions and solidification kinetics. The calculation of the mushy zone's thickness in each time step considers variables such as the volume fraction of liquids and solids, temperature, solute composition, and local solidification time. Initially, the mushy zone is thinner due to higher cooling rates and faster solidification. However, as solidification progresses and the rate of solidification diminishes, the mushy zone thickens. The thickness of the mushy zone diminishes as heat continues to be extracted from the molten metal, causing it to contract towards the end stages of solidification, as more material solidifies.

4. Local temperature was considered as a function of both the liquid concentration composition (ω_l^i) and the liquidus slope (m_l^i).

$$T = T_m + \sum_{i=1}^{N} m_l^i \omega_l^i \quad (4)$$

Here, T_m represents the melting temperature of pure iron, N denotes the number of solute elements present in the steel and m_l^i is the slope of liquidus. The slopes of the solidus and liquidus are linked together by the partition coefficient, defined as:

$$k^i = \frac{m_s^i}{m_l^i} \quad (5)$$

here, m_s^i is the slope of the solidus (derived from a linearized binary phase diagram relative to iron), and k^i represents the partition coefficient to translate the nonhomogeneous repartition of the chemical element i between the solid and the liquid.

5. The solute flux is determined following Fick's law:

$$j = -D_l^i \nabla \omega_l^i \quad (6)$$

D_l^i represents the diffusion coefficient of the chemical element i in the liquid.

6. The heat flux was determined according to Fourier's law, which accounts for the sum of contributions from both natural convection and radiation.

$$q = -\lambda \nabla T.n = h\,(T - T_{ext}) \quad (7)$$

$$h = h_{cv} + \varepsilon_r \sigma_r (T + T_{ext})\left(T^2 + T_{ext}^2\right) \quad (8)$$

in the equation, n represents the outward normal unit vector, h stands for the heat transfer coefficient, and T_{ext} denotes the external temperature. Additionally, ε_r represents the steel emissivity (equal to 0.8), while σ_r stands for the Stefan-Boltzmann constant ($\sigma_r = 5.776 \times 10{-}8$ $Wm^{-2}K^{-4}$). The heat transfer coefficient h changes over time or with variations in the interface temperature between the metal and the mold, allowing for the simulation of contact or detachment (formation of air gap) between the casting and the mold during metal cooling.

7. At the macroscopic scale, diffusion is negligible in the solid phase.
8. At the microscopic scale, the following assumptions were made: i) Thermomechanical equilibrium is maintained at the interface between liquid and solid; ii) Perfect diffusion occurs within the liquid phase; and iii) the Brody-Flemings model is utilized to describe the diffusion process within the solid phase.

$$\omega_s = k\omega_0 \{1 - (1 - 2\alpha k) f_s\}^{(k-1)/(1-2\alpha k)} \quad (9)$$

$$f_s = \left[\frac{1}{(1-2\alpha k)}\right]\left\{1 - \left[(T_f - T)/(T_f - T_l)\right]^{(1-2\alpha k)/(k-1)}\right\} \quad (10)$$

Here, ω_s is the solute concentration at the advancing solid/liquid interface, f_s is the solid fraction, k is the partition coefficient, and α is the Fourier number.

9. The solidification shrinkage is automatically computed using the equation:

$$\Delta\varepsilon_{tr} = \frac{(\rho_l - \rho_s)}{\rho_l} \quad (11)$$

where ρ_s and ρ_l represent densities at the solidus and liquidus temperatures, respectively.

Pure thermal and coupled thermal-mechanical computations are conducted in the simulation by solving various governing equations with a prescribed time step. These computations are performed based on the aforementioned assumptions to analyze fluid flow, temperature, and solute distribution during material solidification. The governing equations utilized in the model are detailed below.

The thermal computation is conducted by solving the general energy conservation equation in heat transfer.

$$\rho\frac{\partial H}{\partial T}\frac{dT}{dt} - \nabla\cdot(\lambda(T)\nabla T) = 0 \quad (12)$$

Here, ρ (kg/m3) denotes the density, T (°C) represents temperature, λ denotes thermal conductivity, and H stands for specific enthalpy, which is defined as follows:

$$\frac{\partial H}{\partial T} = C_p(T) + L_f\frac{\partial f_l(T)}{\partial T} \quad (13)$$

where Cp (J/kg/K) represents the specific heat, f_l denotes the volume fraction of liquid, and L_f (J/kg) stands for the specific latent heat of fusion.

Redistribution of each solute i was controlled by the solute conservation equation.

$$\frac{\partial\omega^i}{\partial t} + \nu\nabla\omega_l^i - \nabla\cdot\left(f_l D_l^i\nabla\omega_l^i\right) = 0 \quad (14)$$

The state of mechanical equilibrium is determined by the momentum conservation equation, which is fundamental in dynamics and signifies the conservation of momentum.

$$\nabla\cdot s - \nabla p + \rho g = \rho\frac{dv}{dt} \quad (15)$$

where s denotes the Cauchy stress tensor, p represents pressure, g stands for gravitational acceleration, and v denotes the average velocity.

To replicate the cooling progression of the material as it shifts from liquid to mushy and then to solid states, a hybrid constitutive model is utilized. The averaged mass balance varies according to the state of the metal.

In the liquid state, the metal exhibits Newtonian behavior and follows the Navier-Stokes equation, incorporating terms that vary with temperature.

$$\overline{\sigma} = \eta_l(T)\sqrt{3}^2\dot{\overline{\varepsilon}} \quad (16)$$

here, $\overline{\sigma}$ represents the Von Mises equivalent flow stress, η_l denotes the dynamic viscosity of the liquid, T stands for temperature, and $\overline{\varepsilon}$ represents the equivalent plastic strain rate.

In a thermo-elasto-viscoplastic treatment of metals below the solidus temperature (Ts), the Lagrangian formulation is often employed. Law II of Kozlowski et al. can be reformulated within this framework to suit the specific conditions of the solid state.

$$\overline{\sigma} = K_s(T)\overline{\varepsilon}^{n(T)}\dot{\overline{\varepsilon}}^{m(T)} \quad (17)$$

in this context, K_s represents the viscoplastic consistency within the solid material, while $\overline{\varepsilon}$ denotes the equivalent plastic strain. The variables n and m correspond to the strain hardening coefficient and the sensitivity coefficient, respectively, which characterize the relationship between the flow stress and the strain rate.

Two distinct behaviors of the metal in the mushy state are distinguished based on a critical temperature known as the coherency temperature T_{conf}, which corresponds to a liquid volumetric fraction $f_l = 0.3$. In the mushy state, the semi-liquid metal is treated as a non-Newtonian fluid following the thermo-viscoplastic Norton-Hoff Law above the temperature T_{conf}.

$$\overline{\sigma} = K^{vp}(T)\sqrt{3}^{m(T)+1}\dot{\overline{\varepsilon}}^{m(T)} \quad (18)$$

where K^{vp} represents the viscoplastic consistency of the material. The strain rate tensor $\overline{\varepsilon}$ is divided into a viscoplastic (non-reversible) component and a thermal component.

The continuity equation (mass conservation equation) is as follows:

$$\nabla.\, v = 3\alpha(T)\dot{T} + \dot{f}_s(T)\Delta\varepsilon_{tr} \quad (19)$$

here, α presents the linear thermal expansion coefficient.

Below the temperature T_{conf}, the semi-solid metal with a low liquid fraction is assumed to follow a thermo-elasto-viscoplastic (EVP) constitutive behavior. This behavior is modeled according to the Perzyna law, which incorporates a threshold type.

$$\overline{\sigma} = \sigma_s + K^{evp}(T)\sqrt{3}^{m+1}\overline{\varepsilon}^n\dot{\overline{\varepsilon}}^m \quad (20)$$

The strain rate tensor $\dot{\varepsilon}$ is decomposed into an elastic component, a visco-plastic component, and a thermal component.

And the continuity equation (mass conservation equation) is as follow:

$$\nabla.\, v = -\left(\frac{\dot{p}}{x} - \frac{\dot{x}}{x^2}p\right) + 3\alpha(T)\dot{T} + \dot{f}_s(T)\Delta\varepsilon_{tr} \quad (21)$$

where, $x = \frac{E}{3(1-2\upsilon)}$, E is the young's modulus, υ is the poisson's coefficient.

The input parameters and thermal boundary conditions are detailed in Tables 7 and 8 of Appendix 1.

2.3.1. Criteria for micro-porosity formation

The possible formation of centerline porosity in the solidification model is based on the Niyama criteria [20,27,34], as expressed in equation (22). It is important to note that the Niyama criteria does not consider the precise size and shape of porosities, but it does enable the prediction of the risk, possibility, and zones of porosity formation when the value exceeds unity [35,36]. The Niyama criterion is mathematically expressed as follows [27,35,36]:

$$Niyama = \frac{\sqrt{\|\dot{T}\|}}{\|\Delta T\|} \quad for\ f_l = f_{lNi} \quad (22)$$

The symbol $\dot{T}$ represents the cooling rate and ΔT denotes the temperature gradient, Additionally, f_l represents the liquid fraction, and f_{lNi} is the threshold liquid fraction set at $f_{lNi} = 0.3$. It is worth noting that the presented Niyama equation is the inverse of the Niyama criterion expression found in some publications [37–39]; therefore, in this work, high criterion values indicate a substantial likelihood of micropore formation.

2.3.2. Macro-porosity formation criteria

The primary (pipe shrinkage) or secondary shrinkage (macro-porosity) was estimated by calculating the volume loss incurred in the

ingot during each step. This volumetric loss is attributed to thermal contraction and the transition from liquid to solid phases. The distribution of this volume loss is determined in accordance with the progression of the solidification front. A threshold solid fraction of 60%, $f_{s_0} = 0.6$, representing the upper limit beyond which the volume loss is deemed irrelevant to the shrinkage process, was used, in agreement with the literature [36,40]. Consequently, the volume loss within the liquid and mushy zones, where the solid fraction is below this threshold, is included in the shrinkage calculation. The computation of volume variation attributable to shrinkage follows equations (23) and (24) [27,35]:

$$\Delta V = \int_{t_1}^{t_2} (\Delta\varepsilon_{tr}\dot{f}_s dt + 3\alpha(T(t))\dot{T})dt \tag{23}$$

$$\Delta\varepsilon_{tr} = -\frac{(\rho_{liquidus} - \rho_{solidus})}{\rho_{liquidus}} \tag{24}$$

The above expression, $[t_1, t_2]$ denotes the current time interval, and $\Delta\varepsilon_{tr}$ signifies the relative change in volume resulting from the complete phase transition between liquidus and solidus. Here, $\rho_{liquidus}$ and $\rho_{solidus}$ represent the respective densities at the liquidus and solidus temperatures. Additionally, $\dot{f}_s$ represents the rate of change of the solid fraction, $\alpha(T(t))$ is the coefficient of linear expansion dependent on temperature, and $\dot{T}$ denotes the rate of change of temperature. The decrease in height for each increment in the shrinkage level is inferred from ΔV in the following manner [27]:

$$\Delta h = \frac{\Delta V}{S} \tag{25}$$

in this context, S represents the surface defined by the solid fraction f_{s_0}.

2.4. Model validation

The model validation process included experimental measurements such as temperature assessments, dye penetration inspection (DPI), and optical emission mass spectrometry chemical analyses. The predicted temporal variations in temperature on the mold's outer surface were compared with the measured values obtained from the TCs, as illustrated in Fig. 1a and detailed in Table 1. After the simulation, temperature measurements on the mold's outer surface were conducted using seven sensors (S1–S7), each corresponding to the thermocouples used in the experiment. These sensors were positioned identically to the experimental setup; for example, sensor 1 (S1) was placed in the same location as thermocouple 1 (TC1). Fig. 5 shows the comparison between the predicted and experimental temperature measurements. In Fig. 5, the initial phase depicts a rapid successive increase in temperature, indicative of the sequential interaction between the molten metal and the mold during the pouring process. Subsequently, this upward temperature trend decelerates due to heat dissipation from the mold wall. Approximately 4.5–5 h after attaining their respective temperature peaks, a decline is observed. Notably, owing to the reduced conductivity of the insulating sideboard within the hot top, the rising temperature trend is tempered, resulting in the lowest peak temperature values recorded by TC1, TC2, and TC3. A clear correlation between the

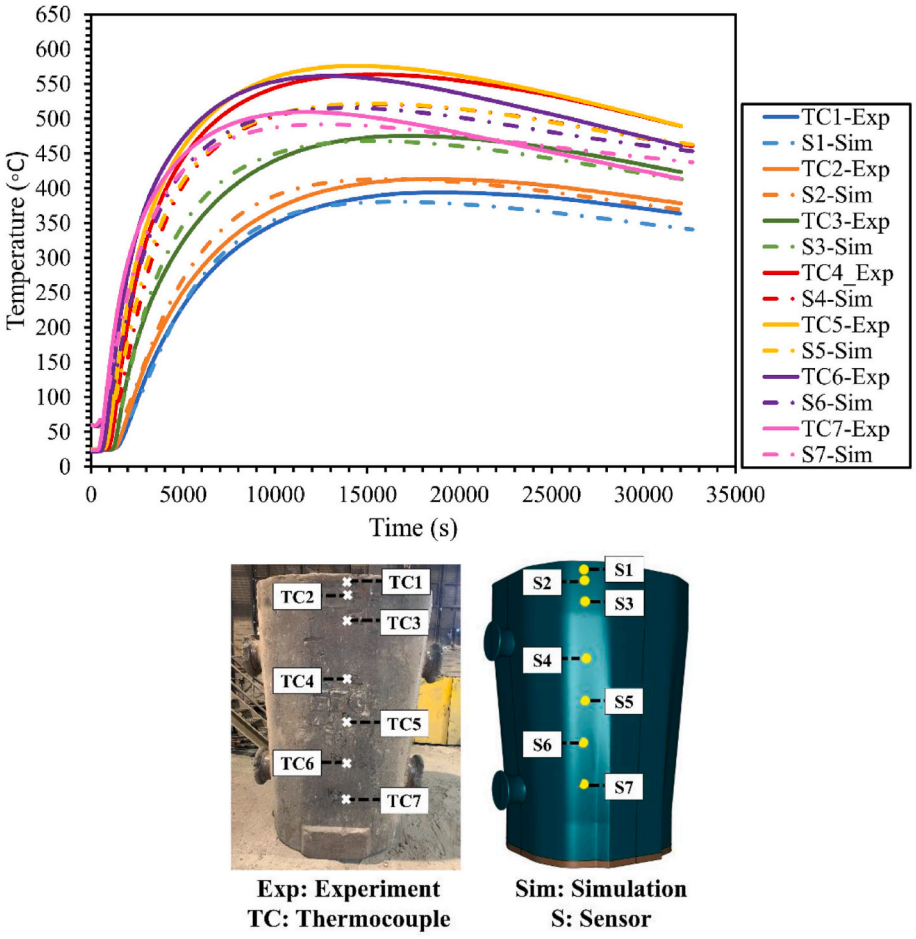

Fig. 5. Temperature profiles on the outer mold surface during solidification for a 12 MT Ingot: comparison between experimental measurements with thermocouples (TC) and predicted temperatures derived from thermomechanical simulation utilizing sensors.

predicted model values and the measured ones is observed, particularly in the hot top zone. The differences observed between the temperatures recorded by thermocouples and those predicted by simulations, which range from 20 to 50 °C, can be ascribed to uncertainties in the precise values of thermal conductivity for both the cast iron mold and the refractory tiles utilized in the computational model. The thermal conductivity of the cast iron mold was obtained from the JMatPro database [27,41] and that of the refractories from the manufacturer data sheet. The thermophysical parameters of the casting setup components, including density and thermal conductivity, are reported in Table 7 of Appendix 1.

After the simulation, the computation of the Niyama value was conducted. Fig. 6 provides a visual representation of the probability and spatial distribution of microporosity formation based on the simulation results. Microporosity is observed at a depth of 1144 mm from the top surface of the hot top part, surpassing the Niyama threshold of 1. These results are in agreement with the dye penetration inspection (DPI) results. In Fig. 3, the presence of microporosity is evident in the centerline blocks on the half longitudinal section of the 12 MT ingot, located at a distance of 1165 mm from the top surface.

Furthermore, the simulation encompassed the computation of the macrosegregation ratio for carbon at various locations, encompassing the top, middle, bottom, and centerline positions. The macrosegregation ratios obtained through simulation were subsequently compared to the corresponding experimental results at identical positions. The details of the comparative analysis serving to confirm the validity of the macrosegregation model, are reported in our previous publication [3,21]. Fig. 7 illustrates the macrosegregation of carbon, comparing simulation results (left) with experimental findings (right) at the end of solidification. Both simulation and experiment indicate the presence of positive segregation at the hot top and negative segregation at the bottom. Additionally, a solute-enriched zone (depicted in yellow) between the wall and center, as well as a depleted solute zone with negative segregation adjacent to the hot top wall, are observed in both the experiment and simulation. The distance from the wall to the conical negative segregation is estimated to be 228 mm and 231 mm in the experiment and simulation, respectively, at the 1/4 ingot body, as shown in Fig. 7. Similarly, these values are measured at 248 mm and 263 mm in the experiment and simulation, respectively, at the 2/4 ingot body. The depth of positive segregation is observed to be 296 mm and 286 mm in the experiment and simulation, respectively. These findings indicate a favorable agreement in the location of positive and negative segregation between the experiment and simulation.

2.5. Influence of hot top geometry

Four distinct scenarios were considered in the present investigation. These scenarios, detailed in Table 2, were devised to bring geometrical modifications that would alter the hot top's thermal regime and mass ratio, defined as the ratio of the hot top melt's weight to the total melt weight. The Original Design (OD), features the reference with a mass ratio of 21.35% (Fig. 8a). The New Designs are named ND1 to ND4 with the following characteristics:

ND1. the mass ratio is reduced to 11.36% by decreasing the hot top height from 381 mm to 181 mm (Fig. 8b).

ND2. the hot top height was increased from 381 mm to 546 mm, the mass ratio from 21.35% to 29%, and the sideboard height from 203 mm to 368 mm (Fig. 8c). The above changes were expected to increase the mass ratio and the average temperature of the hot top.

ND3. the enhancement in the thermal regime of the hot top was further increased by introducing an additional sideboard below the existing one and replacing the material of the upper sideboard with a new one, with lower thermal conductivity (Fig. 8d).

ND4. the hot top height was increased towards the body, accompanied by a reduction in body size (Fig. 8e).

It is noteworthy that the ingot body size remained unchanged for ND1, ND2, and ND3.

3. Result and discussion

3.1. Impact of hot top variations on CET

The THERCAST code used in this study does not explicitly reveal CET. However, it has been reported that CET could be approximated with good precision by considering the relationship between the thermal gradient ahead of the solidification front, the rate of movement of the solidification front, and the solid fraction [17,36]. The above data could be extracted from the simulation and, as described in the following, used to determine the CET in the present study. To anticipate the CET position in the considered designs, the average solidification rate was assessed at the solidification front in the bottom, middle, and top positions of the ingot body for each considered design during solidification, as reported in Fig. 9. Fig. 9a illustrates the positioning of the bottom, middle, and top areas at heights of 253 mm, 790 mm, and 1351 mm, respectively, measured from the ingot's bottom. The rate of solidification, plotted against the solid fraction, generally exhibited a decreasing trend, followed by a minimum and then an increase (Fig. 9b, c, and d). The variation in the hot top resulted in decreased heat extraction during solidification, leading to a reduced solidification rate, particularly noticeable for ND3 and ND4 configurations compared to OD. This contrasts with the outcome for ND1, where the solidification rate increased compared to OD, due to a reduction in hot top height. The inflection point, indicated by an arrow, corresponds to the CET (Fig. 9b, c, and d). These results are in agreement with those reported by Patil

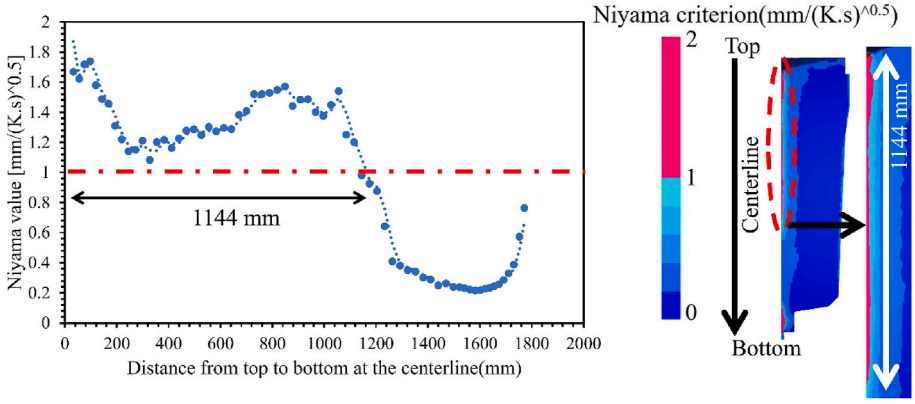

Fig. 6. Predicted risk of microporosity formation at the centerline of the 12 MT Ingot, with the Niyama value criteria illustrated by the red dashed line.

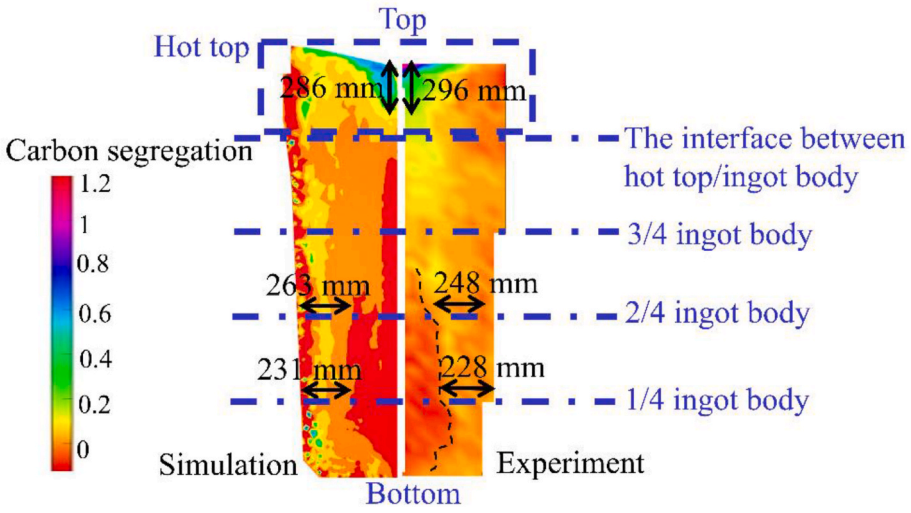

Fig. 7. Macrosegregation pattern of carbon by simulation (left) and experiment (right).

Table 2
Characteristics of investigated design configurations.

Designs	Hot top height	Mass ratio	Sideboard height	Thermal conductivity
OD	381 mm	21.35%	203 mm	1.23 W/m/K
ND1	181 mm	11.36%	203 mm	1.23 W/m/K
ND2	546 mm	29%	368 mm	1.23 W/m/K
ND3	381 mm	19.87%	Top: 203 mm Bottom:177 mm	Top: 0.45 W/m/K Bottom: 1.23 W/m/K
ND4	546 mm	29.5%	406 mm	1.23 W/m/K

et al. [36,40], who also observed such a trend in a 4 MT ingot.

The inflection points observed in Fig. 9 could be explained by the dynamic interplay between solidification rate and thermal gradient, which impact the casing structure. Fig. 10 illustrates the thermal gradient ahead of the solidification front for different positions of the ingot for each of the new designs. It could be seen that the thermal gradient decreased during solidification for all four investigated hot top designs. During the early stages of solidification, a high-temperature gradient and the rapid cooling rate at the mold wall led to the formation of chilled equiaxed grains. Figs. 9 and 10 demonstrate that the thermal gradient and solidification rate peak when the solid fraction is between 10% and 20% for each curve. As solidification progressed, both the temperature gradient and solidification rate gradually diminished towards the ingot's core, a trend expected as solidification remains columnar. This combination of a high thermal gradient and consistent cooling rate from the ingot's surface to its core promotes the growth of columnar grains. In the final stages of solidification, as the thermal gradient ahead of the solidification front decreased, the driving force for the columnar dendritic structure diminished, resulting in an increased rate of solidification. Increasing solidification velocity increases undercooling at the main growth front, also favoring equiaxed growth [18]. This swift solidification, coupled with an elevated cooling rate, generates more nucleation sites for solidification, facilitated by broken dendrite arms serving as nucleation sources. Therefore, the nucleation of new grains is facilitated by more nucleation sites operating at smaller undercooling, as also reported by Straffelini et al. [17], and Patil et al., [36]. The significant increase in nucleation sites results in the formation of an equiaxed structure at the ingot core. The size of the equiaxed grains is governed by solidification rate, alloy composition and its thermodynamics as well as temperature gradient, thereby contributing to the formation of the CET boundary [17,18,36]. Based on the above analysis, it could be said that the inflection point observed in the solidification rate curve corresponds to the CET.

Modifying the hot top configuration resulted in a shift of the CET point towards the ingot center in ND2, ND3, and ND4 due to alterations in solidification conditions, including temperature gradient, solidification rate, and cooling rate. According to the results presented in Table 3, Table 4, and Table 5, the CET occurred up to 46% (in ND3), 58% (in ND2 and ND4), and 70% (in ND4) of solidified shell thickness at the bottom, middle, and top of the ingot, respectively. It must be mentioned that the solidified shell thickness values were estimated from the volume fractions of liquid and solid, calculated by the model during the solidification process. The solidified shell thickness from the mold surface up to the CET position was assessed for every design, with detailed values provided in Tables 3–5. The difference in solidified shell thickness between the OD and each new configuration was calculated for the bottom, middle, and top of the ingot, as illustrated in the locations shown in Fig. 9a. The maximum extension in solidified shell thickness at the CET point amounted to 56 mm, 63 mm, and 60 mm when compared to the OD at the bottom, middle, and top of the ingot, respectively (refer to Table 3, Table 4, and Table 5). Thus, the hot top configuration including mass ratio and thermal regime impacted the final structure and chemical heterogeneities by changing the CET position. The findings revealed that the CET point shifted towards the wall surface with a decrease in mass ratio and hot top height (ND1) and towards the ingot core with an increase in mass ratio, hot top height, and the thermal regime of the hot top, which included using extra insulation and increasing the sideboard height (ND2, ND3, and ND4). These shifts in CET position significantly influenced the chemical composition homogeneity and quality of the final ingot structure, as discussed in subsequent sections.

3.2. *Solidification time criteria*

Solidification time plays a crucial role in the solidification process, influencing both segregation and shrinkage porosity. In instances where the solidification time is too short, feeding towards the ingot centerline is inadequate, while excessive solidification time can lead to severe segregation [22]. Solidification time is influenced by the cooling rate, where a higher cooling rate results in rapid solidification or a shorter solidification time. Therefore, the solidification time impacts shaping microstructural features such as CET, grain size, and dendrite arm spacing [42]. In accordance with Chvorinov, it has been recommended that the solidification time of the feeder should surpass that of the feeding body time. Qian et al. [22] further proposed that the analysis of the solidification process can be translated into the calculation of solidification time by considering all hot top and mold parameters

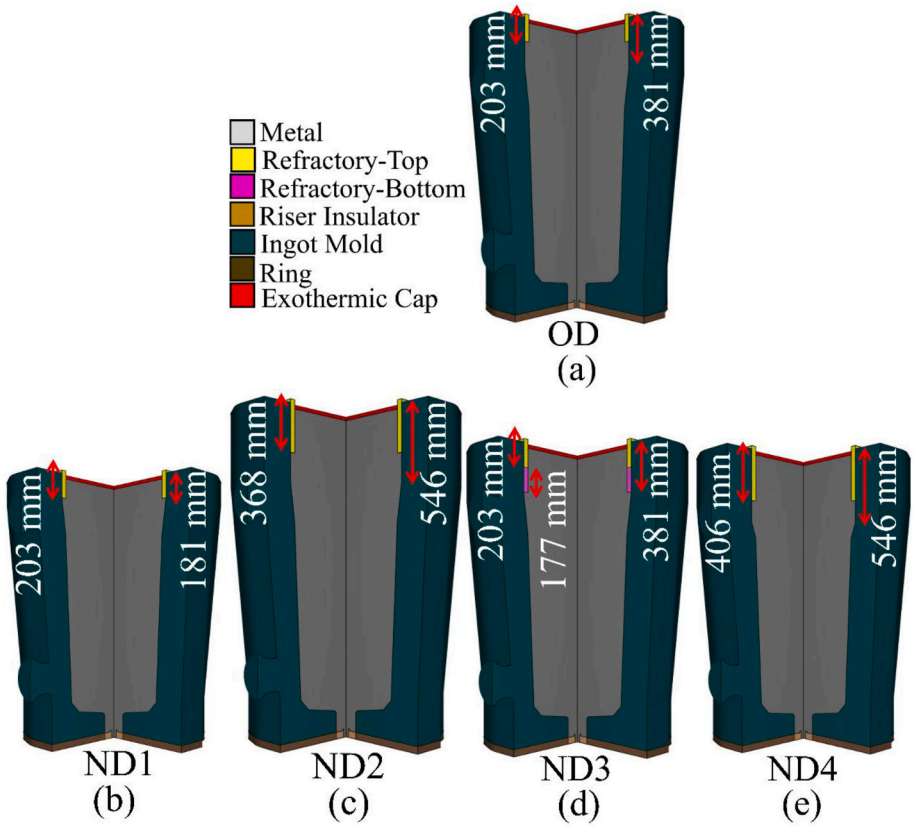

Fig. 8. The investigated designs: (a) OD: original or reference, (b) ND1: reduction of hot top height, (c) ND2: increase in hot top height and sideboard height, (d) ND3: utilizing two refractories, (e) ND4: increase in hot top height towards body.

collectively. Through the design of an appropriate solidification time ratio (t_f/t_b, where t_f is the total solidification time of the hot top, and t_b is the solidification time of the ingot body), they asserted that the determination of hot top parameters for different ingots becomes possible. The researchers identified a suitable range for the $t_f/\ t_b$ value for a 100-ton steel ingot; however, they acknowledged that this value is dependent on factors such as steel grade, pouring process, and ingot weight [22]. The hot top configuration plays a crucial role in influencing factors such as cooling rate, solidification rate, and heat gradient, which collectively impact the overall solidification time. In the present case study, where the hot top's thermal regime and geometry are altered in different configurations, the Total Solidification Time ratio (TST) approach is used for the 12 MT ingot. This proposed criterion aims to serve as a guiding principle for future investigations into hot top design. Table 6 presents the total solidification time for each design, representing the duration from the start of the simulation to reaching the solidus temperature. Generally, the total solidification time, considering both the hot top and the body, increased by approximately 1 h:27min, 1 h:37min, and 1 h:48min in ND2, ND3, and ND4, respectively, while it decreased up to 16 min in ND1 compared to OD. These findings underscore the significant influence of hot top configuration on solidification kinetics. As previously mentioned, CET was extended to 63 mm, 56 mm, and 60 mm in ND2, ND3, and ND4, respectively, while it was shortened to 38 mm compared to OD in ND1. Based on these results, a mere 16-min decrease in solidification time led to a reduction in the length of CET (the distance between CET point and the wall surface) by about 38 mm. Consequently, the decrease in total solidification time resulting from a reduction in hot top volume had a greater impact on the position of CET compared to an increase in total solidification time. This observation underscores the significant impact of solidification time on the positioning of the CET. Even a minor reduction in total solidification time, as little as 16 min, results in a notable decrease, around 21% in CET length.

Subsequently, the total solidification time of the hot top and the body was estimated separately along the centerline, which marks the final position where molten metal solidifies. The TST ratio was calculated by relating the solidification time in the hot top to that in the body ($ratio = \frac{TST_h}{TST_b}$ where TST_h indicates the total solidification time in the hot top and TST_b represents the total solidification time in the ingot body). Fig. 11 illustrates the results of the *TST ratio* for each design at the end of the solidification process ($T_{nominal\ solidus} = 1445\ ^{\circ}C$). Based on the obtained results, the *TST ratio* exhibited values of approximately 1.048, 1.002, 1.335, 1.227, and 1.424 in OD, ND1, ND2, ND3, and ND4, respectively. It was observed that an increase in solidification time correlates with an increase in the TST ratio. The increase in the *TST ratio* confirms that the time required for the solidification of the hot top exceeds that of the body. The specific value of the *TST ratio* varied depending on the type of variation applied to the hot top due to differences in solidification kinetics. To discern which TST ratio signifies a superior ingot quality, the assessment of shrinkage microporosity, shrinkage cavity, and macrosegregation was conducted for each design, as detailed in the next section.

3.2.1. Microporosity and CET

Controlling defects, such as shrinkage porosity, stand as a critical aspect in ensuring the quality of large steel ingots [34]. The observed severe shrinkage porosities along the centerline, with lengths approaching 2 m, underscore the critical role of melt-feeding dynamics in the central casting region and its subsequent impact on shrinkage porosity volume [22,37]. Although the formation mechanism of shrinkage includes heat flow, mass flow, and some other complicated phenomena including solidification contraction, liquid metal movement, alloy segregation, microstructure evolution, and thermal and mechanical stress, but it has been reported that pure thermal calculation

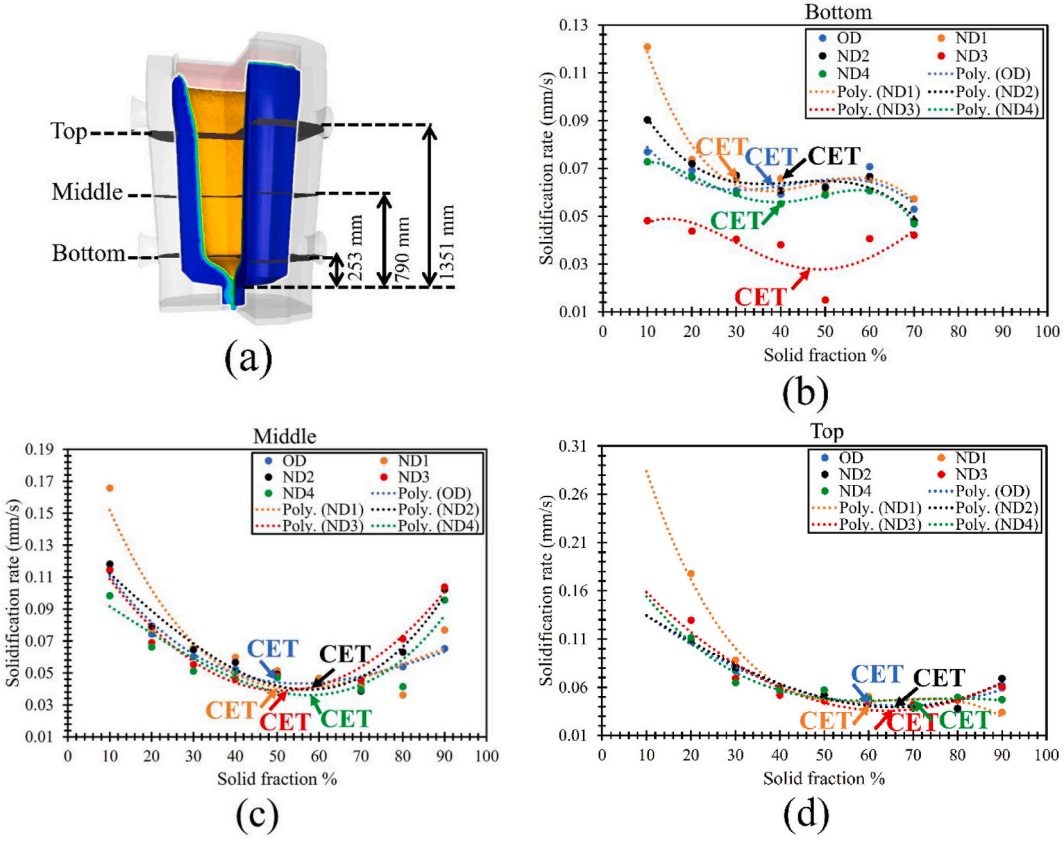

Fig. 9. Solidification rate (mm/s) against solid fraction percentage at different designs, (a) the locations of bottom, middle, and top regions, (b) bottom zone, (c) middle zone, (d) top area.

provides reliable prediction of shrinkage porosity formation [20,27]. In the present work, the Niyama criteria associated with the thermal gradient ahead of the solidification front and the cooling rate were employed for predicting centerline porosity and the results are reported in Fig. 12. Results indicate a lower likelihood of microporosity formation, especially up to 800 mm below the hot top surface in ND2, ND3, and ND4, underscoring the potential benefits of specific hot top configurations in minimizing such defects. Furthermore, Niyama values, up to 1.57, 1.78, 1.5, 1.5, and 1.56 in OD, ND1, ND2, ND3, and ND4, respectively, were reached which offer quantitative insights into the level of risks for microporosity formation.

The correlation between melt-feeding dynamics and the CET is fundamental, as their collective impact shapes the solidification process and resultant microstructure. Effective management of melt feeding has the potential to influence thermal gradients and fluid flow patterns within the ingot during solidification. These factors, in turn, intricately dictate the location and formation time of the CET. Alterations in fluid flow patterns, induced by melt-feeding dynamics, can significantly affect the dispersion of gas and impurities within the solidifying metal. For the ND1 configuration, with its distinct hot top volume, rapid solidification occurred, leading to insufficient melt feeding, resulting in an earlier formation of the CET compared to the OD. This early onset of the CET was associated with an increase in microporosity formation in the centerline. This scenario underscores the critical link between melt feeding dynamics, CET timing, and the occurrence of microporosity.

Fig. 13 presents the Niyama contour for each design, with pink zones indicating potential locations for microporosity formation. The results demonstrate that alterations in hot top configuration influenced the dispersion pattern of microporosity in the centerline. Continuous microporosity is observed in OD and ND1, while ND2, ND3, and ND4 exhibited separated locations with a potential for microporosity formation. Measuring the depth of microporosity in the ingot centerline from the top surface revealed values of 1144 mm, 957 mm, 1374 mm, 1241 mm, and 1177 mm in OD, ND1, ND2, ND3, and ND4, respectively. The continuous microporosity line in the center transited to separated zones with increased solidification time in the different designs. The percentage of the area without the risk of microporosity formation in the dispersion line is calculated as follows:

% Zones without porosity risk in the ingot centerline=((*The length of zones without porosity in the line exposed to porosity formation*)/(*The total length of the centerline exposed to porosity formation*)) × 100.

According to Fig. 14, the percentage of zones without the risk of microporosity formation reaches up to 45%, 43%, and 71% in ND2, ND3, and ND4, respectively.

The percentage calculation in Fig. 14 offers a quantitative perspective on the efficacy of specific hot top configurations in mitigating microporosity. These findings indicate that an 8% increase in the ingot mass ratio and an increase in refractory sideboard height led to decreased cooling rates, temperature gradients, and solidification rates (ND2 and ND4). The longer solidification time, and improved liquid feeding toward the ingot centerline, result in a diminished likelihood of microporosity, contributing to an overall higher ingot quality. Additionally, in the case of ND3, where only the thermal regime was altered by completely covering the hot top, a significant reduction in microporosity formation was observed. The results reported in Figs. 12 and 13 reveal a clear correlation between insufficient insulation in the hot top and the formation of centerline porosities in areas with elevated solidification rates [19].

3.2.2. Shrinkage cavity and CET

The formation of a macroscopic shrinkage cavity occurs in the hot top region due to thermal contraction and the transition from liquid to

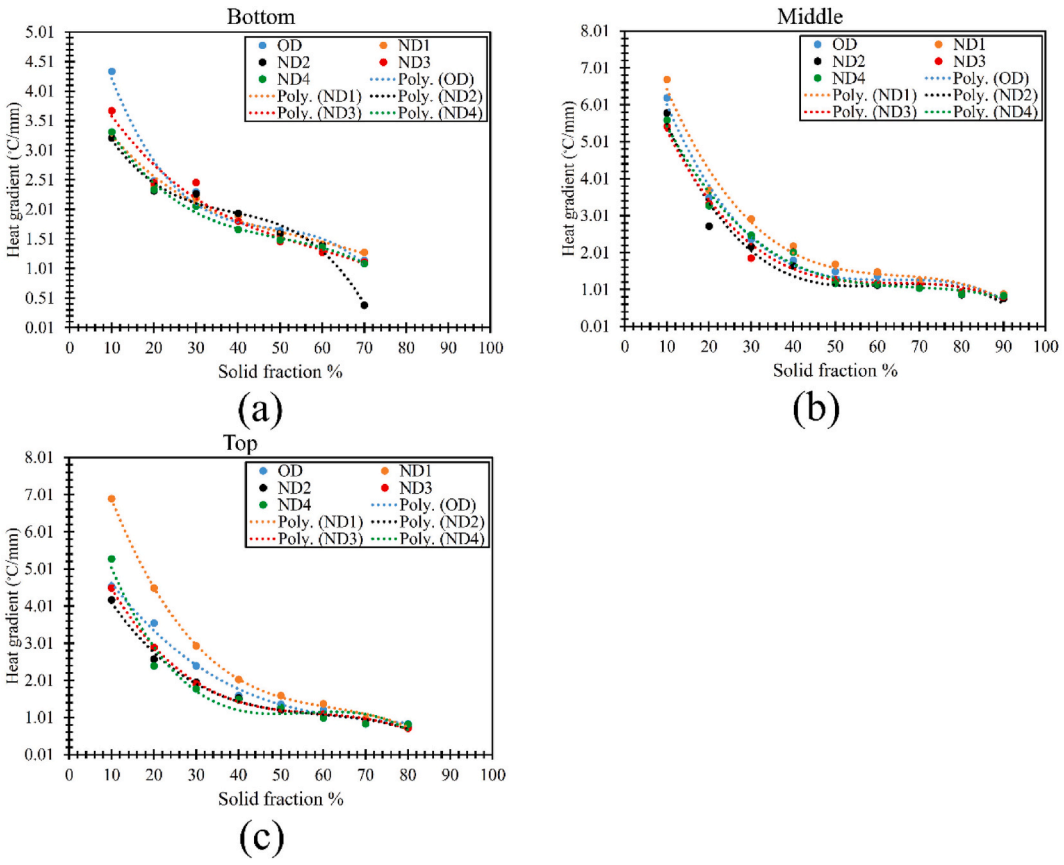

Fig. 10. Heat gradient in the solid front (∘C/s) against solid fraction percentage at different designs at (a) bottom zone, (b) middle zone, and (c) top area, mentioned positioned are shown in Fig. 9a.

Table 3
Solid thickness and solid fraction at the CET position at the bottom.

Bottom		
Designs	CET (percentage of solidified shell thickness)	Solidified shell thickness (mm) up to CET
OD	38 %	179 mm
ND1	30 %	141 mm
ND2	40 %	200 mm
ND3	46 %	235 mm
ND4	40 %	196 mm

Table 4
Solid thickness and solid fraction at the CET position at the middle.

Middle		
Designs	CET (percentage of solidified shell thickness)	Solidified shell thickness (mm) up to CET
OD	50 %	201 mm
ND1	50 %	206 mm
ND2	58 %	264 mm
ND3	53 %	235 mm
ND4	58 %	260 mm

Table 5
Solid thickness and solid fraction at the CET position at the top.

Top		
Designs	CET (percentage of solidified shell thickness)	Solidified shell thickness (mm) up to CET
OD	60 %	239 mm
ND1	60 %	218 mm
ND2	66 %	286 mm
ND3	65 %	280 mm
ND4	70 %	299 mm

Table 6
Total solidification time for each configuration at the end of solidification.

Designs	Total solidification time
OD	5 h:10 min
ND1	4 h:54 min
ND2	6 h:37 min
ND3	6 h:47 min
ND4	6 h:58 min

solid states [35]. The thermomechanical model in THERCAST predicts solidification shrinkage and solid deformation using 3D finite element simulation (as explained in section 2.3.2) [27,29]. Fig. 15 illustrates the shape of the shrinkage cavity for each hot top configuration. The vertical distance from the position of the exothermic cap (where the metal level was in contact with the exothermic cap at the end of filling) to the hot top surface at the end of solidification was measured, resulting in values of 158.2 mm, 141.9 mm, 110.1 mm, 94.4 mm, and 88.92 mm in OD, ND1, ND2, ND3, and ND4, respectively.

Fig. 16 illustrates the cooling rate at the highest point along the centerline of the ingot. The depicted evolution of the cooling rate occurred within the mushy zone, where the liquid fraction ranges between 1 and 0. Variations in the hot top resulted in a reduction in the cooling rate, influencing the depth of the cavity, as observed in Fig. 15. The results show that an increase in solidification time could be

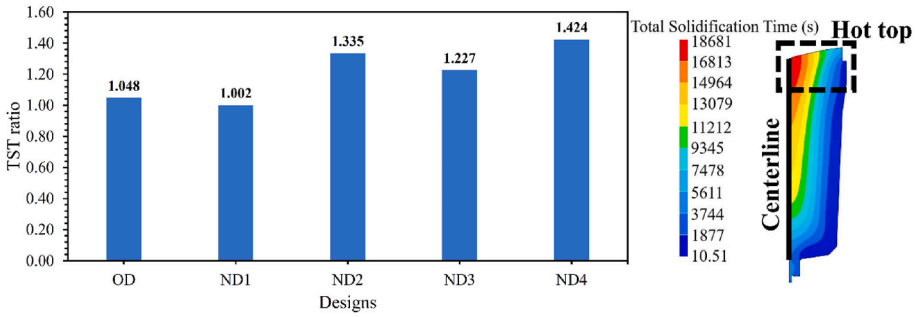

Fig. 11. Ratio of total solidification time (between hot top and body) for each design.

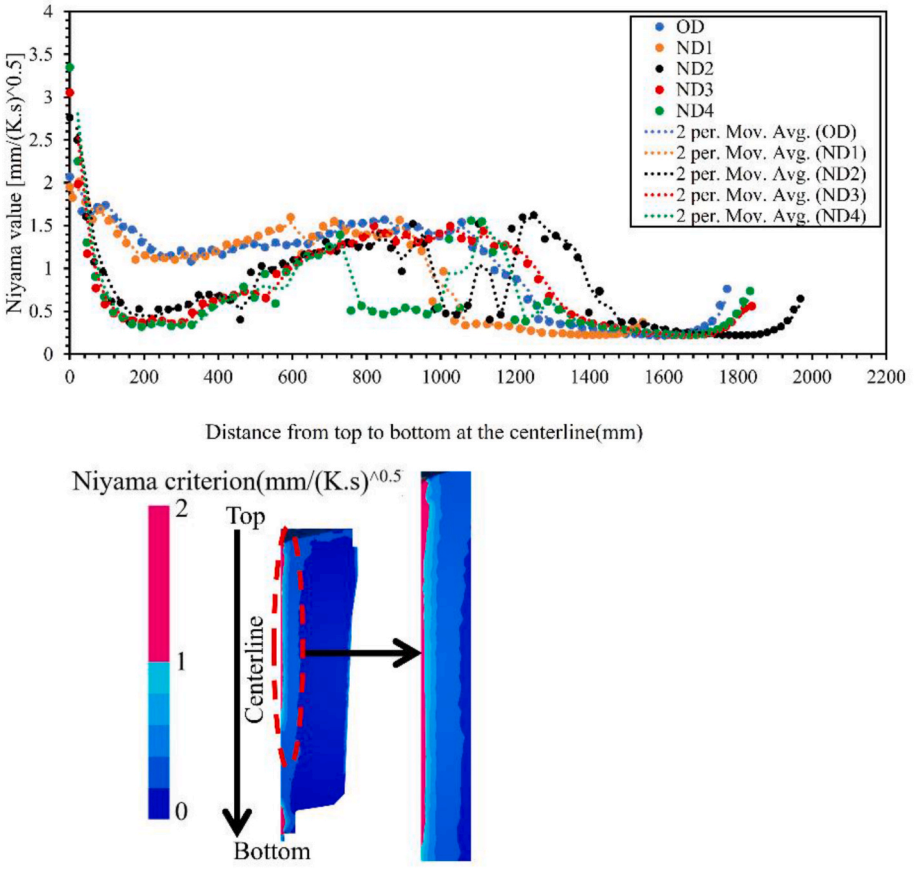

Fig. 12. Predicted risk of microporosity formation at the centerline of the 12 MT Ingot for each configuration.

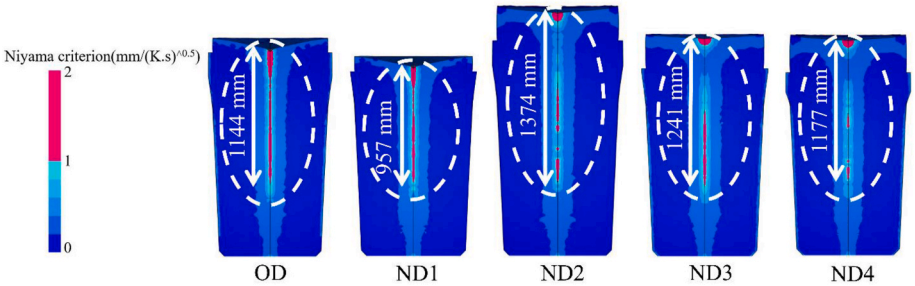

Fig. 13. Risk of microporosity formation along the centerline of the ingot for each design.

correlated with a decrease in the cavity depth. ND4 exhibited the lowest cooling rate and cavity depth according to Figs. 15 and 16. The alterations in the hot top, such as increasing the hot top height and sideboard height, diminished the drop of the metal surface in the hot top region due to reduced cooling rates and prolonged solidification time, consequently prolonging the time needed for the CET occurrence. A

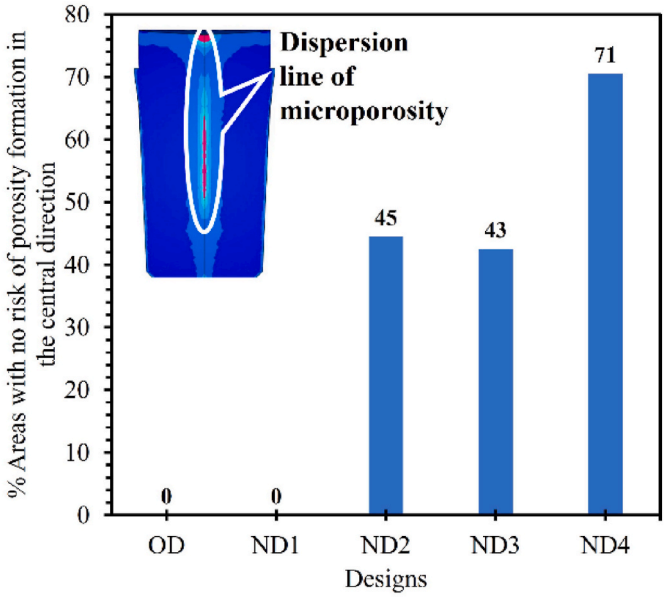

Fig. 14. The percentage of the zones devoid of the risk of microporosity formation along the dispersion line for each design.

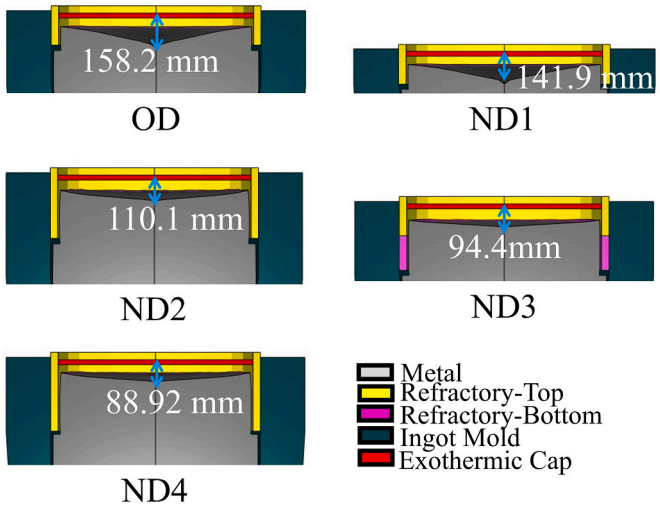

Fig. 15. Surface displacement is caused by shrinkage at the end of solidification in the ingot.

significant shrinkage cavity is commonly associated with uneven solidification rates, cooling gradients, and an early onset of the CET boundary. This can occur due to inadequate thermal insulation of the ingot's hot top. Consequently, the 'timing' of the CET correlates with the depth of the shrinkage cavity in the hot top region. For instance, when the CET occurs near the ingot wall, the depth of the shrinkage cavity in the hot top tends to be greater, whereas, when the CET forms closer to the center of the ingot, the depth of the shrinkage cavity is reduced.

The calculation of the top discarded material resulting from the shrinkage cavity, aimed at flattening the ingot's top surface, is determined using the formula: Waste material in the hot top due to cavity = (Weight of discarded material)/(Total weight of ingot material) × 100. The top discarded material percentages are 5.44%, 5.94%, 3.66%, 3.25%, and 3.05% in OD, ND1, ND2, ND3, and ND4, respectively. In terms of yield material, ND4, ND3, and ND2 show a more efficient use of material compared to OD, as less solid material is wasted due to cropping the shrinkage cavity area. Material usage efficiency was not observed in ND1. Thus, the change in hot top designs contributes to increased material usage efficiency.

3.2.3. Macrosegregation and CET

The thermomechanical solidification model within THERCAST is employed to predict macrosegregation [21,27,35,36,43]. Fig. 17 illustrates the dynamic evolution of carbon macrosegregation percentage and the macrosegregation range (including the maximum and minimum segregation), in the radial direction across the bottom, middle, and top of the ingot for each design (as position indicated in Fig. 9a). Additionally, the CET position is identified for each design in the image. The impact of solidification conditions, attributed to variations in the hot top, is particularly evident in specific radial zones: up to 200 mm from the ingot wall at the bottom, up to 200 mm from the wall and up to 100 mm from the centerline in the middle, and the entire radial direction from the wall to the centerline at the top of the ingot. In the bottom position, all designs exhibit a comparable radial segregation pattern, featuring nearly identical negative segregation ranges. However, ND1, ND2, ND3, and ND4 show less severe segregation near the wall surface compared to OD. Moving to the middle of the ingot, the severity of segregation varies with hot top differences, notably resulting in a reduction in the positive segregation range within 200 mm from the wall surface, especially in ND2 and ND3. At the top of the ingot, there is a discernible increase in the severity of negative segregation in the centerline with an increase in solidification time. The findings suggest that in the context of real ingots, the position of the CET indicates an earlier nucleation of dendritic equiaxed grains in ND1 and OD compared to ND2, ND3, and ND4. Equiaxed grains, denser than the surrounding liquid, tend to sink, driven by convective fluid flow, which is a significant contributor to macrosegregation in large ingots [44]. During the early stage of solidification when the solid front is developing at the bottom of the ingot, which occurs within the first 2 h after pouring the liquid, there is a sufficient volume of liquid pool for fluid movement, ensuring homogeneity of the liquid across all designs. According to the results, the evolution of negative segregation is approximately consistent across different CET positions at the bottom of the ingot. However, during the later stages of solidification, the middle and top sections of the ingot solidify, leading to a reduction in the volume of the molten metal pool, which affects the circulation of fluid. When CET shifts towards the ingot core, the remaining volume for equiaxed grain formation decreases, resulting in reduced homogeneity and increased negative segregation in the centerline. Research indicates that in low-alloy steel ingots, the equiaxed zone at the base of the ingot often contains more globular grains compared to those found further up the ingot. Globular grains are typically rounder and less branched, representing an early stage of equiaxed grain growth before transitioning into dendritic forms [44]. Globular equiaxed grains typically demonstrate lower segregation compared to dendritic equiaxed grains due to their more uniform formation, which diminishes the likelihood of preferential segregation of alloying elements. In contrast, dendritic equiaxed grains possess dendritic arms that can trap segregated solutes during solidification, leading to increased segregation within the grain structure. Therefore, an extended solidification time in ND2, ND3, and ND4 facilitates the transition from globular to dendritic equiaxed grains, consequently increasing centerline negative segregation. However, the prolonged solidification time also diminishes the cooling rate of the mushy zone, allowing more time for solute elements to diffuse in the solid state and resulting in a reduction in positive segregation observed within a distance of up to 200 mm from the surface. Conversely, ND1 exhibits reduced severity of negative segregation at the centerline, attributed to shorter solidification times and the shift of CET towards the wall surface, accompanied by earlier nucleation of equiaxed grains.

Fig. 18 illustrates the macrosegregation patterns at the end of solidification for each configuration, emphasizing the impact of shrinkage on the accumulation of positive segregation. This figure reveals variations in the position and area of positive segregation in the hot top, due to the formation of the shrinkage cavity at the top surface of the ingot. A

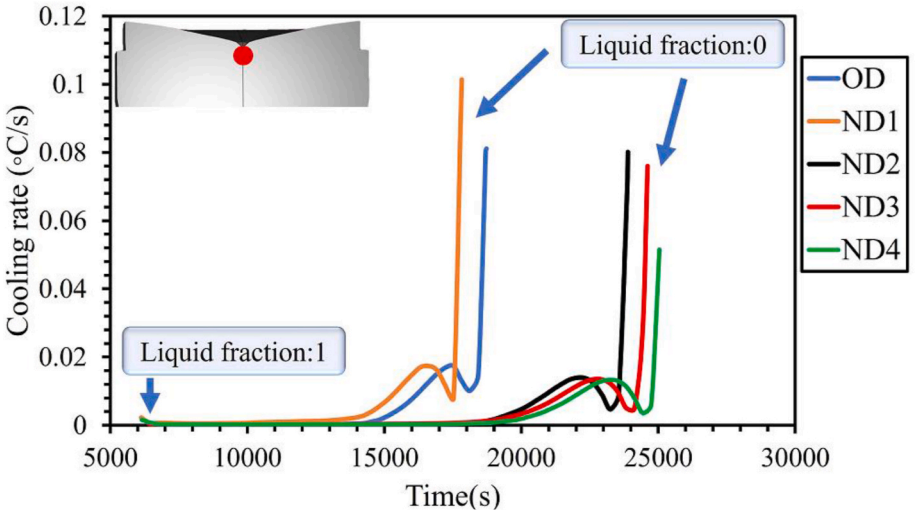

Fig. 16. The cooling rate at the red point is situated at the uppermost position along the centerline of the ingot for each design.

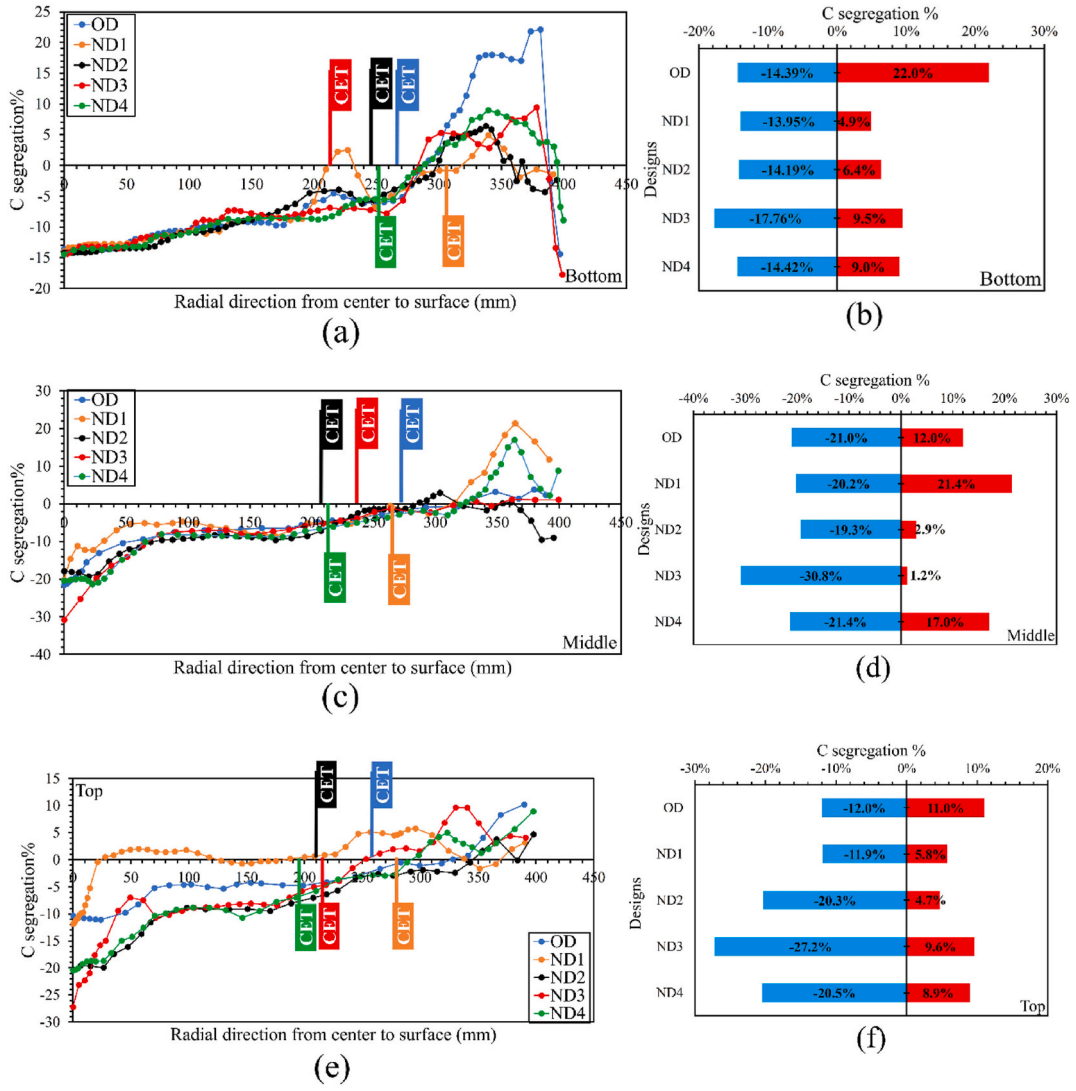

Fig. 17. (a) Evolution of carbon macrosegregation percentage in the radial direction at bottom of the ingot, (b) macrosegregation percentage range of carbon in the bottom of the ingot, (c) evolution of carbon macrosegregation percentage in radial direction at the middle of the ingot, (d) macrosegregation percentage range of carbon in middle of the ingot, (e) evolution of carbon macrosegregation percentage in the radial direction at top of the ingot, (f) macrosegregation percentage range of carbon in top of the ingot. The bottom, middle, and top positions are indicated in Fig. 9a.

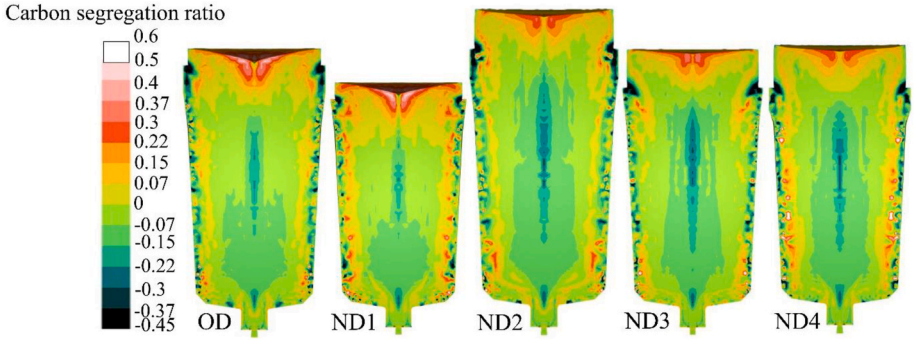

Fig. 18. Macrosegregation pattern of carbon at the end of solidification for each configuration.

reduction in the accumulation of positive segregation is evident in ND2, ND3, and ND4 configurations. Additionally, there is a relocation of positive segregation towards the ingot body in ND1 and OD configurations. Ge et al. [34] reported that shrinkage significantly influences macrosegregation formation in large-size steel ingots, increasing the severity and range of negative segregation in the bottom region. In the hot top area, shrinkage reduces the size of the positive segregation zone and shifts its location to lower regions of the ingot. Therefore, it could be concluded that macrosegregation formation is linked to the CET position and shrinkage cavity formation.

The study's findings (sections 3.2.1 to 3.2.3) underscore the dual impact of prolonged solidification time: a reduction in microporosity along the centerline and the improvement of a shrinkage cavity on the ingot's top surface, accompanied by positive segregation. However, this is countered by an increase in negative segregation along the centerline. This phenomenon is intricately linked to solidification kinetics, encompassing factors such as temperature, cooling rate, solidification rate, the diffusion time of solute elements in the mushy state, and CET position. Notably, during the solid front's development from the wall surface, a high cooling rate hinders solute element diffusion into the solid. In contrast, a lower solidification rate allows for increased diffusion time, promoting homogeneity in the liquid in front of the solid. The centerline, being the last to solidify in the solidification process, plays a crucial role. In the applied thermosolutal convection model for macrosegregation prediction, the fluid movement velocity becomes influential in determining the homogeneity of the remaining liquid in the molten metal. The observed extension in CET position with an increase in solidification time indicates that the columnar region contributes to the occurrence of negative segregation along the centerline. The conclusion of the study recommends a solidification time range between 1.227 and 1.335 to address the various defects considered in this section. A value less than 1.227 suggests underheating in the hot top, inadequate feeding to the central part, and a high cooling rate, resulting in increased microporosity and shrinkage cavity, potentially relocating positive segregation inside the body and decreasing ingot quality. Conversely, a solidification time exceeding 1.335 indicates that CET occurs at a higher solid fraction, leading to an increased length of columnar structure and an elevated risk of negative segregation, particularly in the centerline of the ingot at the middle and the top of the ingot. This conclusion emphasizes the critical importance of selecting an optimal solidification time range to balance defect mitigation and enhance overall ingot quality.

3.3. Molten metal pool and CET

The molten metal pool plays a crucial role in preserving metal temperature throughout the casting process, regulating flow dynamics, achieving alloy homogenization, and influencing microstructural features, including the evolution of the CET [45]. The interaction between the molten metal pool and mold designs significantly influences the solidification process. Careful management of these aspects is imperative for producing high-quality ingots. Understanding the influence of hot top variation on the solidification profile inside the ingot is essential. Fig. 19 illustrates the solidification profile for each configuration at different times after pouring, including 1 h (Fig. 19a), 2 h (Fig. 19b), 3 h (Fig. 19c), and 4 h (Fig. 19d). Dark blue represents the solid phase, red represents the liquid phase, and the colorful area between them depicts the mushy state. Velocity vectors of dynamic fluid within the molten metal pool are represented by arrows, where the arrow size indicates the intensity of fluid flow. The shape of the molten metal changed within the first hour after pouring, with variations in the hot top, particularly in configurations ND2, ND3, and ND4, leading to delayed solidification in the hot top. Consequently, the width of the molten metal pool increased during subsequent hours. The temperature of the molten metal pool influenced the cooling rates, experienced by the solidifying metal. A larger molten metal pool led to slower cooling rates, near the surface of the ingot, potentially delaying the onset of the CET. Fluid flow distribution and intensity varied for different hot top configurations. Convection currents within the molten metal pool affected the distribution of heat and solute within the ingot. This fluid flow influenced the growth morphology of solid grains and, consequently, the CET. Previous studies [34,40] reported a downward fluid flow from the top toward the bottom in the solid front, followed by an upward flow from the bottom toward the top in the centerline. This observed flow pattern can be ascribed to the temperature gradient between the mold wall and the ingot core. The lower temperature near the ingot surface causes an increase in the density of the liquid metal, whereas the liquid metal in the core remains at a higher temperature and lower density. This temperature difference sets in motion a convective loop, influencing the direction of fluid flow during the initial stages of the solidification process. This behavior was observed up to 1 h after pouring. Beyond this point, fluid dynamics primarily moved from top to bottom in the centerline, then turned upward in the solid front. As the solidification process developed, the volume of molten metal decreased, and, influenced by shrinkage effects at the top surface, high-intensity fluid flow was directed from top to bottom in the centerline. The molten metal pool acted as a reservoir to compensate for solidification shrinkage. This affected the distribution of stress within the ingot and, in turn, influenced the formation of shrinkage cavity and the position of the CET. In configurations ND2, ND3, and ND4, especially at 3 h and 4 h after pouring, the larger liquid pool width provided more space for fluid circulation, resulting in increased homogeneity and upward movement of accumulated impurities in the upper region. Additionally, the velocity vector magnitude is higher in these locations due to elevated temperatures. The CET position extended toward the center in ND2, ND3, and ND4.

The dimensions of the liquid metal pool, specifically the height and width, at 1 h, 2 h, and 3 h after pouring were measured (Fig. 20). Notably, ND2, ND3, and ND4 exhibited an expansion in the width of the liquid pool due to increased insulation in the hot top. Specifically, in ND3, the width of the molten metal pool increased by up to 58 mm, 156

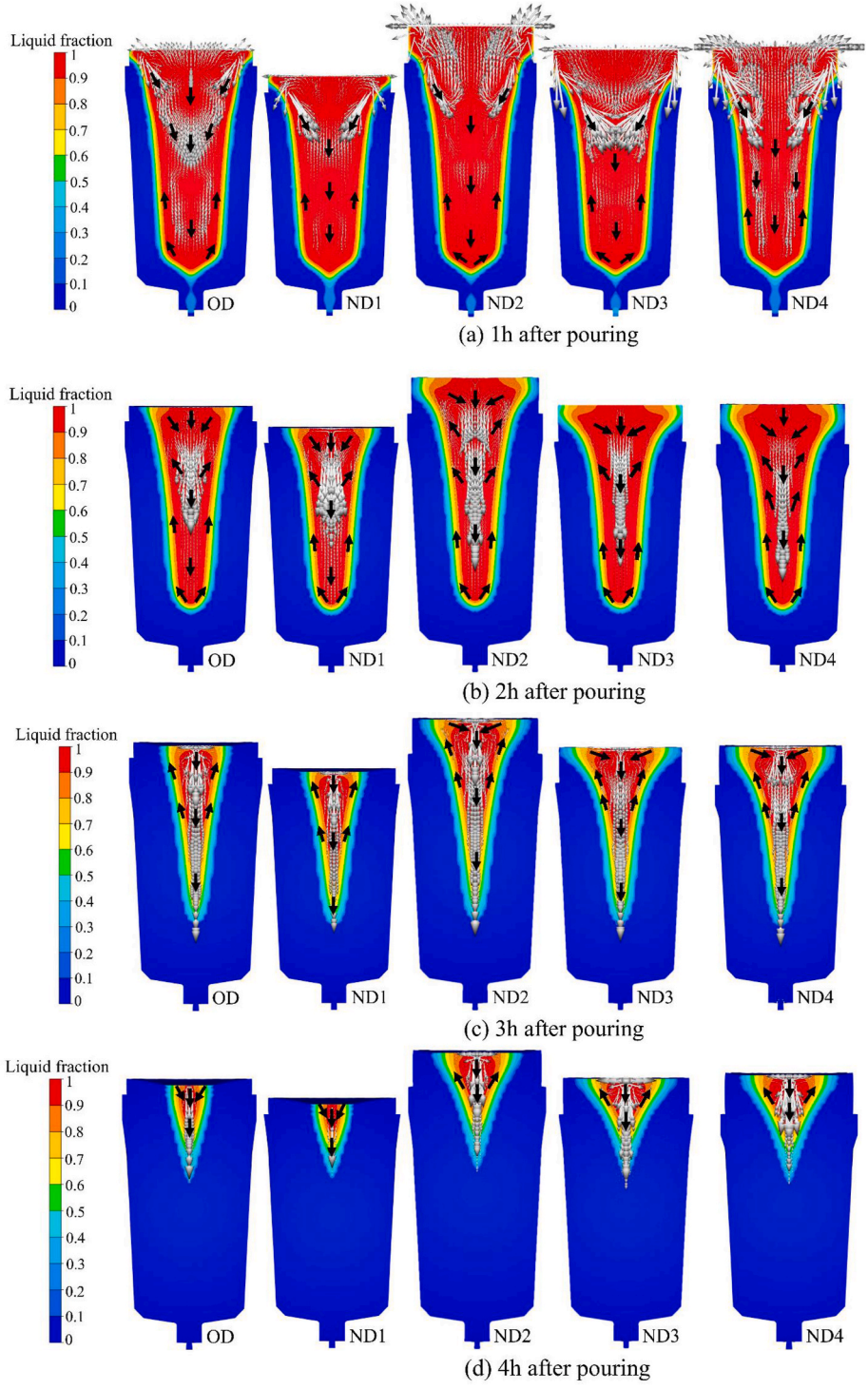

Fig. 19. Liquid fraction and velocity vector of fluid flow for each design, (a) 1 h after poring, (b) 2 h after pouring, (c) 3 h after pouring, and (d) 4 h after pouring.

mm, and 235 mm at 1 h, 2 h, and 3 h after pouring, respectively, compared to the OD configuration. The height of the liquid pool remains relatively stable in ND3 compared to OD. This expansion in width had significant implications for the solidification process, indicating a more extensive area for fluid flow and extended CET position. An increase in the height of the liquid pool was observed in ND2, reaching up to 158 mm, 154 mm, and 82 mm at 1 h, 2 h, and 3 h after pouring, respectively, compared to OD. This variation in liquid pool dimensions was attributed to the alterations in the hot top's structural dimensions. The observed changes in the height of the liquid pool in ND2 further emphasize the role of hot top design in shaping the solidification profile. Overall, these measurements contribute to a comprehensive assessment of how hot top variations influence the molten metal pool, shedding light on the intricate dynamics that govern the different stages of solidification.

Fig. 21 depicts the mushy zone thickness at the bottom, middle, and top of the ingot at the CET point for each design. The image revealed that the thickness of the mushy state increased with an extended solidification time. However, the increase in mushy state thickness was limited,

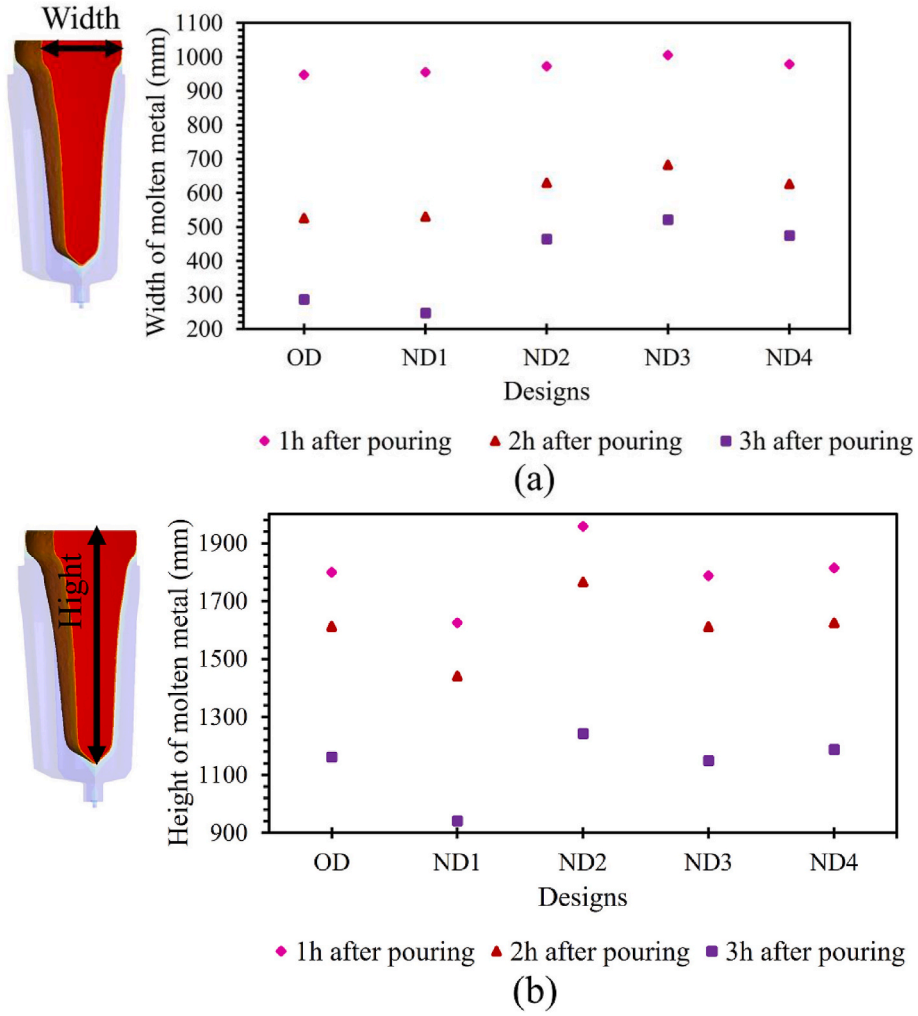

Fig. 20. (a) Width of the molten metal, (b) hight of the molten metal at 1 h (h), 2 h (h), and 3 h (h) after pouring.

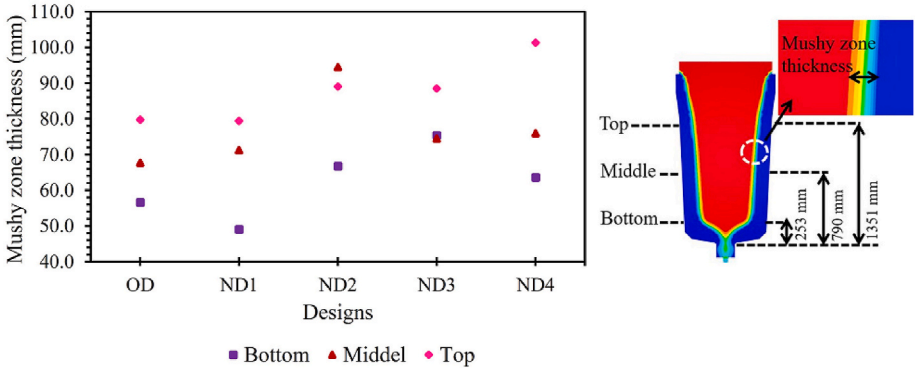

Fig. 21. The mushy zone thickness at the CET point in the bottom, middle, and top of the ingot for each design.

reaching up to 19 mm, 27 mm, and 22 mm at the bottom, middle, and top of the ingot. Consequently, the impact of mushy thickness on defects such as segregation formation is deemed less significant compared to the influences of cooling rate, solidification time, diffusion time, and fluid movement.

4. Conclusions

In this study, the impacts of hot top thermal and geometrical variations on the Columnar-to-Equiaxed Transition (CET) position were investigated. We delved into the significance of solidification time, as a crucial factor in the casting process, and proposed a solidification time criterion tailored for 12 MT ingots. The following conclusions can be drawn from the present work:

- Variations in the hot top configuration, which include geometry and thermal regime, significantly influence the CET position. These variations impact solidification kinetics, such as solidification rate and thermal gradient ahead of the solidification front, thereby causing variations in solid thickness at the CET point. Differences of up to 56 mm, 63 mm, and 60 mm compared to the OD were observed at the bottom, middle, and top positions of the ingot, respectively.
- A solidification time criterion (TST ratio), which relates the solidification time in the hot top to that in the body, is proposed to predict defect formation. A TST ratio below 1.227 indicates increased sensitivity to microporosity and shrinkage cavity formation, while a value exceeding 1.335 raises the risk of negative segregation, particularly in the centerline of the ingot, due to CET occurring at a higher solid fraction. This highlights the importance of optimizing solidification time to improve the overall quality of the ingot.
- The interactions between hot top variations and solidification dynamics during the casting of a 12 MT ingot were quantified. The analysis showed that by a judicious design of the hot top, it was possible to achieve a substantial width increase in molten metal pool, up to 235 mm, within 3 h after pouring.

Declaration of competing interest

The authors declare that they have no known competing financial interests or personal relationships that could have appeared to influence the work reported in this paper.

Acknowledgments

This research received support from the Natural Sciences and Engineering Research Council of Canada (NSERC) under the Collaborative Research and Development project (CRD), Grant number 536444-18. Finkl Steel-Sorel Co. for providing the material is greatly appreciated.

Appendix 1

Table 7
Input parameters for the simulation [3].

Property	Unit	Value	Reference
Filling time	min	26	[46]
Initial temperature of mold and mold components	°C	60	[46]
Exterior environmental temperature	°C	20	[46]
Pouring temperature	∘C	1580	[46]
Superheat temperature	∘C	78	[41,46]
Liquidus temperature	∘C	1502	[41]
Flow rate for 90° symmetry model	mm3/s	265,385	[46]
Energy of ignition of two exothermic caps	MJ	72	–
Number of mesh of the ingot and the components of the mold	–	746,196	–
Mesh size	mm	30	–
Mesh refinement	mm	15 and 8	–
Reference density (steel)	kg/m3	6.93e-6	[28,41]
Melting temperature of pure iron	°C	1540	[28]
Thermal expansion coefficient	1/K	8.853e-5	[28]
Latent heat of fusion	kJ/kg	265	[28]
Emissivity	–	0.8	[28,29]
Density (cast iron)	kg/m^3	7000	[28]
Thermal conductivity (cast iron)	W/m/K	30	[28]
Density (refractory)	kg/m^3	2353	[28,29]
Thermal conductivity (refractory)	W/m/K	1.2	[28,29]
Density (riser insulator)	kg/m^3	868	[28]
Thermal conductivity (riser insulator)	W/m/K	0.45	[28]
Density (exothermic cap)	kg/m^3	500	[28]
Thermal conductivity (exothermic cap)	W/m/K	0.2	[28]

Table 8
Thermal boundary condition of the simulation [3,21,28].

Thermal boundary condition	
Heat transfer coefficient between metal/mold	$h = 5 \times 10^3$ W/m^2.K
Heat transfer coefficient between cast iron mold/outside	$h_{cv} = 12$ W/m^2.K $T_{ext} = 20$ °C
Heat transfer coefficient between metal/refractory and metal/riser	$h = 1 \times 10^2$ W/m^2.K
Thermal resistance at the interface between metal/cap	$R = 1 \times 10^{-5}$ m^2.K/W
Thermal resistance between mold components	$R = 1 \times 10^{-6}$ m^2.K/W
Thermal resistance between mold/refractory and mold/riser material	$R = 1 \times 10^{-2}$ m^2.K/W
Emissivity	0.8
Thermal conductivity of the mold	30 W/m/K
Thermal conductivity of the riser insulator	0.45 W/m/K

References

[1] Wu M, Ludwig A, Kharicha A. Simulation of As-cast steel ingots. Steel Res Int 2018; 89(1):1700037.

[2] Von Schweinichen P, et al. Effect of different casting parameters on the cleanliness of high manganese steel ingots compared to high carbon steel. Metall Mater Trans 2013;44:5416–23. https://doi.org/10.1007/s11661-013-1949-7.

[3] Ghodrati N, et al. Influence of hot top height on macrosegregation and material yield in a large-size cast steel ingot using modeling and experimental validation. Metals 2022;12(11):1906.

[4] Rogotovsky AN, Shipelnikov AA, Bobyleva NA. Modeling and development of a forging ingot of rational design and mass. Journal of Chemical Technology and Metallurgy 2018;53(5):936–42.

[5] Li J, et al. A review on prediction of casting defects in steel ingots: from macrosegregation to multi-defect model. J Iron Steel Res Int 2022;29(12):1901–14. https://doi.org/10.1007/s42243-022-00848-7.

[6] Hurtuk DJ. Steel ingot casting. Casting; ASM Handbookvol. 15. Materials Park, OH, USA: ASM International; 2008. p. 911.

[7] Ahmadein M, et al. Prediction of the as-cast structure of Al-4.0 Wt Pct Cu ingots. Metall Mater Trans 2013;44:2895–903.

[8] Pineda D, Martorano MdA. Columnar to equiaxed transition in directional solidification of inoculated melts. Acta Mater 2013;61(5):1785–97. https://doi.org/10.1016/j.actamat.2012.12.002.

[9] Kwapisiński P, Wołczyński W. Control of the CET localization in continuously cast copper and copper alloys' ingots. Arch Foundry Eng 2023;23:91–9.

[10] Lan P, Zhang J. Numerical analysis of macrosegregation and shrinkage porosity in large steel ingot. Ironmak Steelmak 2014;41(8):598–606. https://doi.org/10.1179/1743281213Y.0000000172.

[11] Ludwig A, Wu M, Kharicha A. On macrosegregation. Metall Mater Trans 2015;46: 4854–67.

[12] Cai D, et al. Modelling of inclusion effects on macrosegregation in solidifying steel ingot with a multi-phase approach. Metall Mater Trans 2019;50(3):1323–32.

[13] Ge H, et al. Modelling of ingot size effects on macrosegregation in steel castings. J Mater Process Technol 2018;252:362–9.

[14] Ge H, et al. Numerical simulation of A-segregation evolution in a 55-ton ingot using four-phase solidification model. Metall Mater Trans B 2021;52(5): 2992–3003.

[15] Khalajzadeh V, Beckermann C. Simulation of shrinkage porosity formation during alloy solidification. Metall Mater Trans 2020;51:2239–54. https://doi.org/10.1007/s11661-020-05699-z.

[16] Wu M, Ludwig A, Kharicha A. A four phase model for the macrosegregation and shrinkage cavity during solidification of steel ingot. Appl Math Model 2017;41: 102–20.

[17] Straffelini G, et al. Modeling solidification microstructures of steel round billets obtained by continuous casting. ISIJ Int 2011;51(9):1448–53. https://doi.org/10.2355/isijinternational.51.1448.

[18] O'Reilly K. Solidification and casting: an Oxford–Kobe materials Text. CRC Press; 2016.

[19] Tashiro K, et al. Influence of mould design on the solidification and soundness of heavy forging ingots. Transactions of the Iron and Steel Institute of Japan 1983;23 (4):312–21. https://doi.org/10.2355/isijinternational1966.23.312.

[20] Wang J, et al. Shrinkage porosity criteria and optimized design of a 100-ton 30Cr2Ni4MoV forging ingot. Mater Des 2012;35:446–56. https://doi.org/10.1016/j.matdes.2011.09.056.

[21] Ghodrati N, et al. Influence of the hot-top thermal regime on the severity and extent of macrosegregation in large-size steel ingots. Journal of Manufacturing and Materials Processing 2024;8(2):74.

[22] Qian S, et al. Hot top design and its influence on feeder channel segregates in 100-ton steel ingots. Mater Des 2015;87:205–14. https://doi.org/10.1016/j.matdes.2015.07.150.

[23] Kermanpur A, et al. Influence of mould design on the solidification of heavy forging ingots of low alloy steels by numerical simulation. Mater Des 2010;31(3): 1096–104.

[24] Kumar, A., et al. Experimental and Numerical Studies of the influence of hot top conditions on Macrosegregation in an industrial steel ingot. in *Proceedings of the first international conference on ingot casting, rolling and forging (IRCF)*. Juin 2012. Aachen, Allemagne, pp 3-7.

[25] Li H-c, et al. Effects of hot top pulsed magneto-oscillation on solidification structure of steel ingot. China Foundry 2018;15:110–6. https://doi.org/10.1007/s41230-018-7198-z.

[26] MATLAB. MATLAB and statistics toolbox release 2012b. Natick, MA, USA: The MathWorks, Inc.; 2012. 2012b.

[27] Transvalor SA. Cedex, France, *THERCAST® NxT 2.1, USER MANUAL, ingot casting*. 2017. Transvalor.

[28] TherCast2.1®. TherCast 2.1®, Transvalor, S.A., Cedex, France. 2021.

[29] Zhang C, et al. Influence of thermomechanical shrinkage on macrosegregation during solidification of a large-sized high-strength steel ingot. Int J Adv Des Manuf Technol 2018;99:3035–48.

[30] Zhang C, et al. FE modelling and prediction of macrosegregation patterns in large size steel ingots: influence of filling rate. Metals 2022;12(1):29. https://doi.org/10.3390/met12010029.

[31] Beckermann C. Modelling of macrosegregation: applications and future needs. Int Mater Rev 2002;47(5):243–61.

[32] Lesoult G. Macrosegregation in steel strands and ingots: characterisation, formation and consequences. Mater Sci Eng, A 2005;413:19–29.

[33] Zhang C. Influence of casting process parameters on macrosegregation in large size steel ingots using experimentation and simulation. École de technologie supérieure. Quebec City, QC, Canada: University of Québec; 2020.

[34] Ge H, et al. Four-phase dendritic model for the prediction of macrosegregation, shrinkage cavity, and porosity in a 55-ton ingot. Metall Mater Trans 2017;48: 1139–50.

[35] Ghodrati N, et al. Modeling of the influence of hot top design on microporosity and shrinkage cavity in large-size cast steel ingots. In: 8th International congress on the science and technology of steelmaking; 2022. p. 239–44. https://doi.org/10.33313/531/031. Montréal, QC, Canada.

[36] Patil P, et al. Improvement in quality and yield of the low alloy steel ingot casting through modified mould design. Trans Indian Inst Met 2017;70(8):2001–15.

[37] Abootorabi A, Korojy B, Jabbareh MA. Effect of mould design on the Niyama criteria during solidification of CH3C 80t ingot. Ironmak Steelmak 2019:722–30.

[38] Zhang Y, et al. Effects of weight-compatible design on ingot solidification. Steel Res Int 2021;92(3):2000560.

[39] Liu N, et al. Effect of electromagnetic induction coil position on feeding effect in steel ingot. AIP Adv 2022;12(4).

[40] Patil P, et al. Analysis of solidification behaviour of low alloy steel ingot casting–simulation and experimental validation. Ironmak Steelmak 2015;42(7): 512–24. https://doi.org/10.1179/1743281214Y.0000000256.

[41] Sente. Software.Ltd, *JMatPro user's guide*. 2005.

[42] Ferreira AF, et al. Effect of pouring temperature on microstructure and microsegregation of as-cast aluminum alloy. Int J Adv Des Manuf Technol 2019; 104(1):957–65. https://doi.org/10.1007/s00170-019-03979-6.

[43] Ghodrati, N., et al. Influence of Hot Top Geometry on the Solidification Time and Macrosegregation in Large-Size Cast Ingot Using Finite Element Modeling. in *the 62nd Conference of Metallurgists, COM 2023*. 2023. Toronto, Ontario, Canada: Springer, Cham, p. 477-480. https://doi.org/10.1007/978-3-031-38141-6_65.

[44] Pickering EJ. Macrosegregation in steel ingots: the applicability of modelling and characterisation techniques. ISIJ Int 2013;53(6):935–49.

[45] Ridolfi MR. The formation of the solidification microstructure from liquid metal in industrial processes. In: Materials science forum. Trans Tech Publ; 2017.

[46] Finkl-Steel-Sorel, http://www.*sorelforge.com/*.